ISSN: 3023 - 8609

VOLUME 2, ISSUE 2, JULY 2025

AN INTERDISCIPLINARY JOURNAL OF MEDICAL TECHNOLOGIES

COMPUTERS AND ELECTRONICS IN MEDICINE

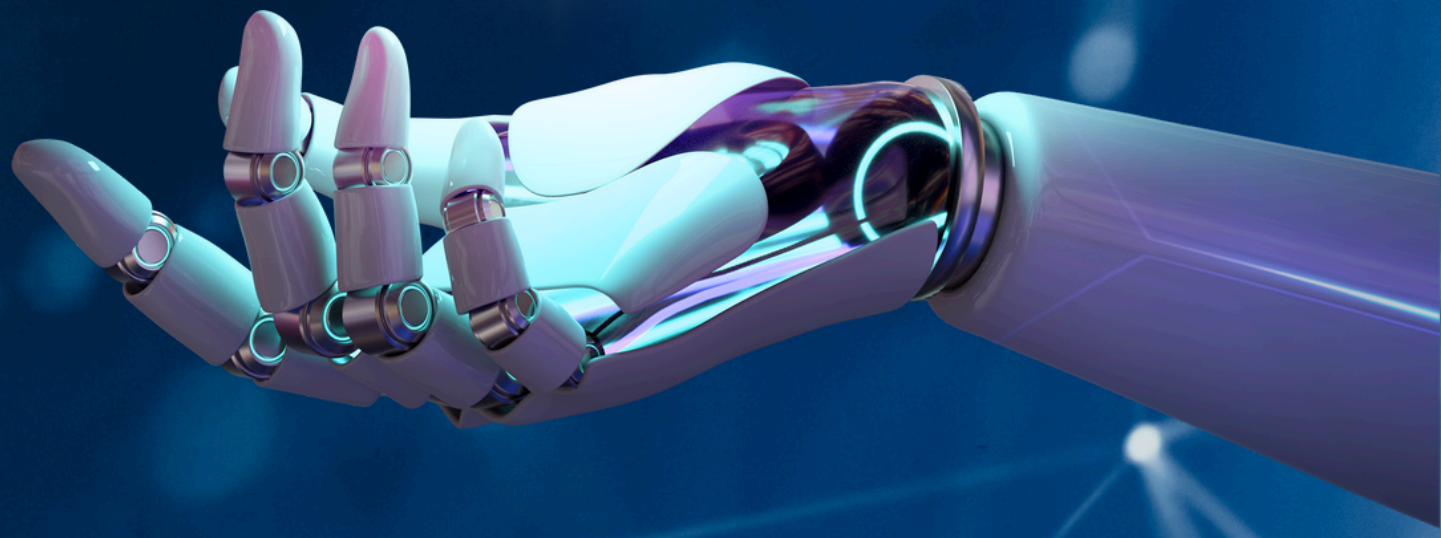

ADBA

https://journals.adbascientific.com/cem

ISSN: 3023-8609

Computers and Electronics in Medicine
Volume: 2 – Issue No: 2 (July 2025)

EDITORIAL BOARD

ISSN: 3023-8609

Computers and Electronics in Medicine
Volume: 2 - Issue No: 2 (July 2025)

CONTENTS

https://journals.adbascientific.com/cem/issue/view/14

ADBA
Computers and Electronics in Medicine
Cutting-Edge Scientific Solutions

e-ISSN: 3023-8609
RESEARCH ARTICLE
Vol.2 / No.2 / 2025 / pp.26-35
https://doi.org/10.69882/adba.cem.2025071

Deep Learning in Robot-Assisted Surgery: A Conceptual Framework for the da Vinci System

Hakan Özcan *,[1]
*Department of Computer Technology, Design Vocational School, Amasya University, Amasya, 05100, Türkiye.

ABSTRACT This study proposes a conceptual framework for integrating deep learning into the da Vinci Surgical System. The framework was developed after identifying common applications and challenges through a systematic review. It combines multiple data types, including visual, kinematic, and physiological signals, into a closed-loop system. This system includes four core components: data acquisition and fusion, deep learning-based analysis, adaptive control and feedback, and continuous skill assessment. These components interact to support real-time surgical guidance and personalized training, aiming to improve surgical outcomes. To inform the framework, a systematic search of the PubMed database was conducted, focusing on studies that combine deep learning with the da Vinci system. Two major application areas were identified: the first involves autonomous or semi-autonomous instrument control and image-guided navigation, and the second covers surgical skill assessment and workflow analysis. While existing studies demonstrate the potential of artificial intelligence in robotic surgery, they also reveal technical and practical limitations. By analyzing these common approaches and obstacles, this study provides a structured foundation for future research. The proposed framework offers a unified view that connects data processing, intelligent decision-making, and feedback, paving the way for smarter systems that assist both in real-time procedures and long-term training, and helping bridge the gap between advanced robotic hardware and cognitive support in surgical environments.

KEYWORDS
Artificial intelligence
Deep learning
Robotic surgery
Robot-assisted surgery
da Vinci System
Conceptual framework
Decision support system

INTRODUCTION

In recent years, advances in surgical technology have significantly transformed patient care and operative procedures. Robot-assisted surgery (RAS) now enables surgeons to perform complex interventions with enhanced precision, reduced invasiveness, and improved efficiency (Reddy *et al.* 2023). These innovations have contributed to better clinical outcomes, including shorter recovery times, reduced postoperative complications, and increased procedural consistency (Kinoshita *et al.* 2022; Saman 2024). As a result, robotic systems have become a central feature in many surgical specialties (Cannizzaro *et al.* 2024).

A particularly important development in this field is the integration of advanced decision-support technologies into RAS platforms (Iftikhar *et al.* 2024). Artificial intelligence (AI), and more specifically deep learning (DL) techniques, have emerged as critical components of this evolution (Panesar *et al.* 2019). These techniques are capable of processing complex, multi-modal datasets to support real-time intraoperative decision-making, analyze surgical performance, and predict patient-specific risks (Egert *et al.* 2020). Recent studies emphasize that the convergence of robotic systems with AI has the potential to enhance intraoperative safety, personalize surgical strategies, and improve outcomes by extending the surgeon's capabilities beyond mechanical precision alone (Iftikhar *et al.* 2024; Knudsen *et al.* 2024).

One of the most prominent platforms in RAS is the da Vinci Surgical System, developed by Intuitive Surgical in the late 1990s and first introduced into clinical practice in 1999 (Pugin *et al.* 2011). Now used in hospitals worldwide, the da Vinci system has become a cornerstone of minimally invasive surgery (Azizian *et al.* 2020; DiMaio *et al.* 2011). It integrates surgeon-controlled robotic arms with an ergonomic console and a high-definition (HD), 3-dimensional

Manuscript received: 10 May 2025,
Revised: 9 July 2025,
Accepted: 14 July 2025.

[1]hozcan@amasya.edu.tr (**Corresponding author**).

(3D) endoscopic imaging platform, enabling precise replication of the surgeon's hand movements with enhanced dexterity and tremor filtration (Cepolina and Razzoli 2022; Pugin *et al.* 2011). This setup allows for careful tissue handling and suturing through small incisions, improving surgical precision and supporting faster patient recovery (Cepolina and Razzoli 2022). The system's design provides a stable, immersive view of the operative field and facilitates complex procedures with greater control and better outcomes compared to conventional minimally invasive techniques (Steffens *et al.* 2023). Its 3D visualization significantly enhances spatial orientation and depth perception, which is essential for performing intricate procedures with minimal trauma to surrounding tissues (Koh *et al.* 2018). Over the past two decades, the da Vinci Surgical System has demonstrated substantial clinical impact across multiple specialties, particularly urology (Koukourikis and Rha 2021), gynecology (Li *et al.* 2022), and general surgery (Celotto *et al.* 2024). It has also served as a key research and training platform through initiatives such as the da Vinci Research Kit (dVRK), which has fostered innovation and collaboration in the field of surgical robotics (D'Ettorre *et al.* 2021).

Building on this established success, it becomes clear that the next frontier for RAS lies in augmenting these systems with advanced decision-support capabilities. Despite significant technological progress, a notable gap remains in the systematic and clinically validated integration of AI-driven systems into RAS workflows (Boal *et al.* 2024). While DL models have shown potential in interpreting large-scale visual, kinematic, and physiological data for intraoperative guidance (Knudsen *et al.* 2024), current research is often isolated to specific tasks, limited to controlled settings, or lacking cross-platform generalizability. Moreover, a unified architectural framework that integrates these diverse data modalities into a cohesive real-time support system is still lacking, despite the need for adaptable and validated solutions in evolving robotic surgery (Marcus *et al.* 2024). This fragmentation not only hampers clinical translation but also limits opportunities for scalable training, consistent evaluation, and adaptive surgical assistance.

To address this gap, the present study conducts a systematic literature review to examine thematic application domains where DL is employed to enhance various aspects of RAS with the da Vinci system. The review provides a detailed analysis of these applications and identifies persistent challenges hindering clinical integration. Building on these insights, the study proposes a conceptual framework for a multi-modal surgical decision support system (DSS). This framework integrates diverse data streams, including visual, kinematic, and physiological inputs, into a unified closed-loop system designed to support real-time decision-making and continuous surgical skill assessment.

By synthesizing recent advances and outlining future directions, this study aims to contribute to the development of intelligent, adaptive, and data-driven RAS platforms, ultimately facilitating more effective and personalized patient care.

MATERIAL AND METHODS

In order to identify the core components of a conceptual framework, a systematic literature review was conducted following the PRISMA guidelines (Preferred Reporting Items for Systematic Reviews and Meta-Analyses) (Page *et al.* 2021). Predefined inclusion and exclusion criteria were applied to select recent studies focused on DL applications in robotic surgery using the da Vinci Surgical System. The study design is illustrated in Figure 1. Selected studies were grouped by application domain, and key challenges were identified within each group. Based on these insights, a conceptual framework for a multi-modal surgical DSS was proposed to unify the identified components into a cohesive system.

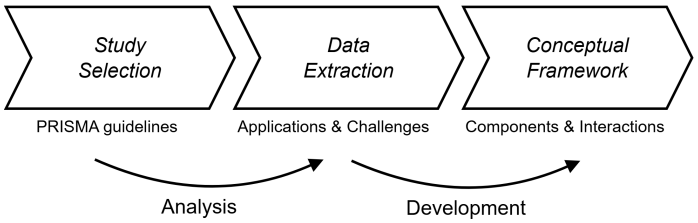

Figure 1 Study design

Study Selection

Initially, 23 publications related to the da Vinci Surgical System and DL applications were retrieved from the PubMed database using the query shown in Figure 2. Predefined inclusion and exclusion criteria guided the study selection. Specifically, studies focusing exclusively on RAS and DL or machine learning applications with the da Vinci Surgical System, published within the last five years and written in English, were included. During the abstract screening, three studies were excluded because they used da Vinci system outputs solely for classification model building or diagnostic support, without directly addressing robotic surgery. After full-text review, one additional study was excluded for not being directly related to robotic surgery or the da Vinci system. In total, 19 studies met the inclusion criteria and were incorporated into the review.

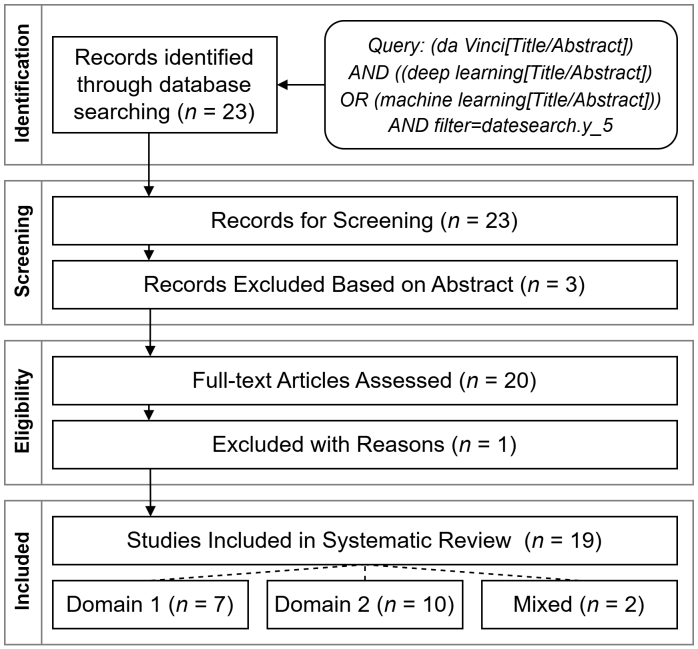

Figure 2 Study selection flow

Data Extraction and Analysis

Following PRISMA guidelines, the findings of each study were systematically summarized and analyzed. Methodological approaches, technologies utilized, and key outcomes were compared. The review was performed in two stages: first, the studies were grouped according to their application domains; then, each group

was re-examined to identify specific challenges in applying DL, which were organized into subtopics.

Conceptual Framework Development

Finally, based on the insights gained from these studies, a conceptual framework for a multi-modal surgical DSS was proposed. This framework is designed to integrate multi-modal data streams from visual, kinematic, and physiological sources into a unified, closed-loop system that supports both surgical decision-making and continuous skill improvement. The framework is intended to serve as a foundation for future research and development in RAS DSSs.

RESULTS AND DISCUSSION

This study, guided by the PRISMA methodology outlined in the methods section, synthesizes current research on the integration of DL into the da Vinci Surgical System. Based on analysis of the selected studies, two primary domains of application have been identified. The first involves autonomous or semi-autonomous instrument control and image-guided navigation, where DL techniques are applied to enhance intraoperative decision-making, visual guidance, and robotic manipulation. The second focuses on surgical skill assessment and workflow analysis, highlighting how machine learning algorithms, combined with physiological and performance data, are used to evaluate surgical proficiency, monitor ergonomics, and support training. As illustrated in Figure 3, there has been a steady growth in the number of studies across both domains, with a noticeable increase in research addressing mixed implementation approaches in recent years. The following sections explore each of these domains in detail, emphasizing the transformative role of DL in RAS.

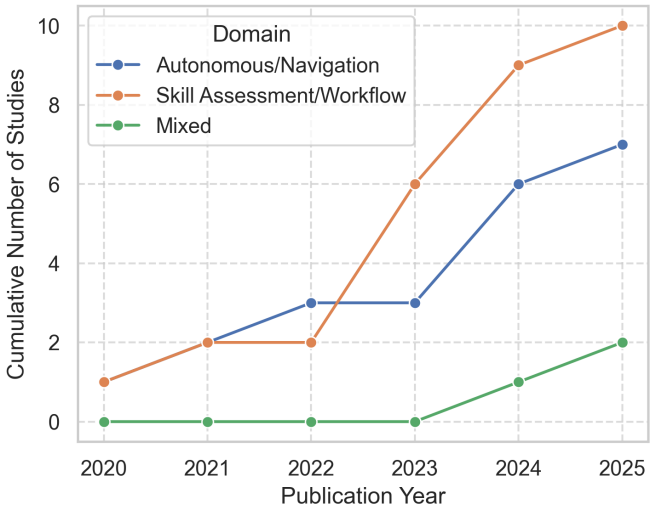

Figure 3 Cumulative deep learning–related *da Vinci* studies by domain (2020–2025)

Autonomous or Semi-Autonomous Instrument Control and Image-Guided Navigation

The integration of DL into the da Vinci Surgical System has led to significant advancements in autonomous and semi-autonomous robotic capabilities, particularly in the realms of real-time visual guidance, instrument control, and tactile perception. Relevant studies on autonomous and semi-autonomous instrument control and image-guided navigation are given in Table 1. These innovations are increasingly contributing to enhanced surgical precision, improved safety, and more efficient intraoperative workflows.

One of the most impactful developments involves real-time 3D model registration and augmented reality (AR)-based navigation. This was demonstrated in a study (Amparore *et al.* 2024) that leveraged the da Vinci system to enhance robotic partial nephrectomy by automatically overlaying patient-specific 3D kidney models onto the surgeon's live endoscopic view. Two complementary approaches were explored. The first utilized computer vision techniques, enhanced by indocyanine green (ICG) fluorescence imaging, to segment kidney structures and establish landmark-based registration. The second approach employed a convolutional neural network (CNN) to automatically detect and segment the kidney directly from live endoscopic images, without relying on fluorescence. Both methods were integrated into the da Vinci system via the TilePro multi-input display, enabling real-time AR guidance during surgery. The reported co-registration times ranged from 7 to 11 seconds, with only minimal manual adjustments required. This automatic overlay system improves intraoperative visualization, supports precise surgical navigation, and reduces cognitive load on the operating surgeon.

Another key area of innovation is camera motion estimation in dynamic surgical environments, which is essential for developing intelligent camera systems. This challenge was addressed in a study (Huber *et al.* 2022) that proposed a DL approach for estimating laparoscopic camera motion using deep homography networks. The researchers created synthetic surgical sequences by introducing artificial camera motion into static da Vinci video frames and used these sequences to train a neural network based on ResNet-34. The proposed system was able to estimate camera motion accurately, even in the presence of moving instruments and tissue, significantly outperforming classical computer vision techniques such as SURF combined with RANSAC. The method achieved up to 41% higher precision and was approximately 43% faster on standard central processing units (CPUs). This capability lays the foundation for intelligent and adaptive camera control systems that can autonomously adjust viewpoint and maintain optimal visual context during complex procedures.

In the domain of skill transfer and task automation, a study (Gonzalez *et al.* 2021) used the dVRK as one of four robotic platforms in the development of the Dexterous Surgical Skill (DESK) dataset. The DESK dataset was designed to enable machine learning models to generalize across different robotic systems and environments, supporting the development of semi-autonomous capabilities in settings such as remote or battlefield surgery. Using the dVRK, the researchers performed a peg transfer task that was broken down into modular surgical gestures, referred to as "surgemes", such as grasping, transferring, and releasing pegs. Detailed kinematic data, including gripper state, position, and orientation, were recorded and used to train classification models. Remarkably, machine learning models trained exclusively on simulation data were able to achieve an accuracy of 93% when tested on real robotic executions using the da Vinci system. This result underscores the potential for leveraging virtual training environments and simulated data to develop generalizable models for real-world autonomous surgical applications.

Another important line of research involves enhancing the realism of biomechanical simulations used in training and preoperative planning. This was demonstrated in a study (Wu *et al.* 2020) that used the dVRK platform in combination with an RGB-depth

Table 1 Studies on autonomous and semi-autonomous instrument control & image-guided navigation

Study	Focus	Methodology/Algorithm	Modalities
(Wu *et al.* 2020)	Simulation correction in soft-tissue modeling	Modified 3D-UNet for correction factor prediction	RGB-D and kinematics
(Gonzalez *et al.* 2021)	Surgeme classification via transfer learning	Supervised learning (RF, SVM, MLP) with FFT features	Kinematics and annotated video images
(Huber *et al.* 2022)	Laparoscopic camera motion extraction	DNN-based homography estimation (using synthetic augmentation)	Laparoscopic surgery video images
(Amparore *et al.* 2024)	3D virtual model overlay in robotic partial nephrectomy	ICG-enhanced computer vision + CNN-based kidney segmentation	RGB endoscopic images (± NIRF) & 3D kidney models
(Ullah *et al.* 2024)	Fluorescence-guided tumor margin delineation	Comparison of visible vs. NIR probes; AI/ML for probe design	Visible and NIRF imaging
(Yilmaz *et al.* 2024)	Sensorless haptic feedback	Disturbance observer with deep learning dynamic compensation	Motor kinematics and force data
(Khan *et al.* 2025)	ML-based tension measurement	LSTM-based torque estimation	dVRK kinematics and force data

Abbreviations: 3D-UNet, Three-Dimensional U-Net; AI/ML, Artificial Intelligence / Machine Learning; AR, Augmented Reality; CNN, Convolutional Neural Network; dVRK, da Vinci Research Kit; DNN, Deep Neural Network; FFT, Fast Fourier Transform; ICG, Indocyanine Green; LSTM, Long Short-Term Memory; MLP, Multi-Layer Perceptron; NIRF, Near-Infrared Fluorescence; RF, Random Forest; RGB-D, Red Green Blue + Depth; SVM, Support Vector Machine.

camera sensor to capture visual and kinematic data while physically interacting with soft-tissue phantoms. They employed this real-time data to improve Finite Element Method (FEM)-based soft tissue models. Specifically, the authors train a neural network to learn the difference between the FEM's predicted tissue shape and the actual tissue shape, as measured by real-time camera and robot data (vision and kinematics). The network then generates a correction factor that adjusts the FEM output to more closely reflect the true, observed deformation of the soft-tissue phantom. The resulting hybrid model reduced simulation errors by 15–30%. These advances underscore the importance of increased realism in soft-tissue simulation, both for surgical training and for machine learning systems that depend on accurate virtual environments to learn complex surgical tasks.

The challenge of providing direct haptic feedback in the da Vinci system has been widely recognized, as tactile information is critical for safely manipulating delicate tissues. This issue was addressed in a study (Yilmaz *et al.* 2024) that implemented sensorless haptic feedback using internal dVRK signals such as joint positions, velocities, and motor torques. In this study, DL is used to estimate the robot's internal dynamics so the system can accurately distinguish external forces (e.g., contact with tissue or surgical objects) from the robot's own motion. Specifically, the authors train a Long Short-Term Memory (LSTM)-based neural network on the dVRK's joint positions and velocities to learn friction and inertia, then subtract this modeled disturbance from the measured motor torque to estimate external contact forces. This sensorless approach provides the basis for haptic feedback. Two experimental tasks were conducted. The first involved tumor detection via palpation, where sensorless feedback increased detection accuracy by approximately 30% compared to visual-only guidance and nearly matched the performance of systems using physical force sensors. The second task focused on the classic peg transfer evaluation, where sensorless feedback significantly reduced unwanted interaction forces by approximately threefold, improving safety and surgical control. Additionally, dynamic modeling contributed to a better user experience by reducing both physical strain and cognitive workload. Importantly, this technique required no additional hardware, highlighting its practical value for improving haptics in existing surgical systems.

In a related effort to enhance intraoperative safety, researchers (Khan *et al.* 2025) developed a machine learning-based method for measuring tissue tension during robotic surgery using the dVRK. Their approach involved using standard da Vinci instruments to apply pulling forces on porcine colon tissues. A LSTM network was trained on kinematic data (joint positions and velocities) and successfully predicted tissue tension with an average accuracy of 74%, reaching up to 88% in optimal cases. The correlation between predicted and ground-truth forces was consistently strong, with Spearman's correlations ≥ 0.81 in four of five experiments (mean ≈ 0.80). By enabling real-time monitoring of tissue stress, this method offers a way to prevent complications such as anastomotic leaks and opens new possibilities for quantitative intraoperative guidance.

Furthermore, emerging research is increasingly leveraging advanced fluorescence imaging modalities to support surgical decision-making. A recent review (Ullah *et al.* 2024) discussed the potential synergy between novel fluorescent probes, near-infrared imaging windows, and robotic platforms in fluorescence imaging-guided surgery. This work emphasized that future directions could include "fluorescence-guided da Vinci" systems, where DL potentially augments the fluorescence signal to provide automated tissue differentiation or tumor margin detection. Taken together with ICG-based AR, as demonstrated in the study (Amparore *et al.* 2024), these developments pave the way for even more sophisticated guidance strategies that seamlessly blend AI-driven analytics, robotics, and real-time imaging to enhance surgical precision.

Overall, these studies demonstrate how DL techniques, when integrated with the da Vinci Surgical System's visual and kinematic data, are pushing the boundaries of robotic surgery. From enhancing visual guidance through AR to predicting physical interactions with tissue, these developments are gradually transforming the da Vinci platform into a more autonomous and intelligent surgical assistant capable of supporting complex intraoperative tasks with greater safety, accuracy, and adaptability.

Surgical Skill Assessment and Workflow Analysis

The da Vinci Surgical System plays a central role in the development of objective, data-driven approaches to surgical skill assessment and intraoperative workflow analysis. Relevant studies focusing on surgical skill assessment and workflow analysis are presented in Table 2. Leveraging its precise motion tracking, real-time data capture capabilities, and compatibility with physiological monitoring systems, the da Vinci platform has enabled the integration of AI-based methods into both surgical training and evaluation environments.

A study (Egert *et al.* 2020) emphasize the foundational role of the da Vinci system in capturing automated performance metrics, such as instrument motion and camera positioning. These quantitative indicators of surgeon performance serve as inputs for machine learning algorithms that can assess surgical proficiency and even predict patient outcomes based on observed patterns. In addition to procedural logging, the da Vinci system supports training through playback features that allow trainees to review expert-performed tasks. These recordings can also be physically re-experienced via tactile robotic control, facilitating the development of procedural muscle memory and enhancing motor skill acquisition. These capabilities suggest that AI-integrated robotic platforms could provide standardized, objective feedback in surgical education.

Several studies have explored the integration of physiological and behavioral monitoring with the da Vinci system to assess surgical skill levels. One example of this approach is a study (Shafiei *et al.* 2024b) that predicted Robotic Anastomosis Competency Evaluation metrics during vesico-urethral anastomosis. The authors collected electroencephalography (EEG) and eye-tracking data from 23 participants performing procedures on plastic models and animal tissue using the da Vinci system. These data were used to train machine learning models, including random forest and gradient boosting regression, which could accurately predict subtask-level performance such as needle handling, tissue trauma, and suture placement. The ability to distinguish performance differences among surgeons of varying experience levels underscores the potential of using physiological and visual metrics for precise, objective skill assessment.

Complementary research (Takács *et al.* 2024) examined the stress and ergonomic impact of RAS with the da Vinci Xi while surgeons performed standardized tasks on a Sea Spikes phantom. Using digital sensors that captured heart-rate variability, posture, and hand movements, the authors trained machine learning models to classify self-reported workload levels and novice versus expert status from these physiological indicators. Preliminary findings suggest that, although the da Vinci's ergonomic design reduces physical strain relative to open surgery, remote tele-operation introduces distinct cognitive and stress-related challenges that differ between novice and experienced surgeons. This insight supports incorporating stress monitoring and ergonomics into future training and evaluation models.

The combined use of EEG and eye-tracking data was further explored in another study (Shafiei *et al.* 2023b) involving live animal surgeries using the da Vinci system. Surgeons performed cystectomy, hysterectomy, and nephrectomy procedures while their physiological responses were recorded during subtasks such as blunt dissection and tissue retraction. Skill levels were assigned using the modified Global Evaluative Assessment of Robotic Skills (GEARS) tool, and models such as multinomial logistic regression, random forest, and gradient boosting were trained to classify surgical expertise. The gradient boosting model achieved classification accuracies up to 93%, demonstrating the reliability of this multimodal approach for distinguishing skill levels in real-time surgical environments.

Building on this line of inquiry, an integrated EEG and eye-tracking study (Shafiei *et al.* 2024a) using eXtreme Gradient Boosting (XGBoost) evaluated mental workload across various simulator- and Fundamentals of Laparoscopic Surgery-based tasks in RAS. This study recruited 26 participants performing Matchboard and Ring Walk exercises on a da Vinci simulator, as well as Fundamentals of Laparoscopic Surgery pattern cut and suturing tasks. The XGBoost models achieved R^2 values above 0.80 for each task and identified key predictors such as pupil diameter, temporal-lobe functional connectivity, and task complexity. These findings further underscore the growing role of advanced physiological analytics in understanding surgeons' cognitive demands and optimizing training programs to improve overall performance.

Reliable model development also depends on high-quality, synchronised data, as demonstrated in a study (Hashemi *et al.* 2023) that outlined protocols for acquiring and processing da Vinci surgical data-combining stereoscopic endoscopic video with surgeon-movement recordings from depth cameras. The researchers further extracted event-level information such as clutch usage and instrument activation by means of computer-vision algorithms. Their open-source pipeline, together with a discussion of commercial recorders like dVLogger, provides a comprehensive framework for dataset development that supports reproducible and automated surgical performance evaluation.

The effectiveness of visual metrics was demonstrated in a study (Shafiei *et al.* 2023a), where participants performed robotic procedures on live pigs while wearing eye-tracking devices. Visual behavior during subtasks such as cold dissection and tissue retraction was analyzed and used to train a gradient boosting classifier, which achieved up to 96% accuracy across different tasks. Expert evaluations using GEARS served as the ground truth. These findings demonstrate that visual metrics collected during da Vinci-assisted procedures can reliably distinguish between varying skill levels, making eye-tracking a practical tool for real-time feedback and objective assessment.

The impact of automated feedback on learning was examined in a study (Brown and Kuchenbecker 2023) involving the da Vinci Standard system and a Smart Task Board. Trainees were divided into feedback and control groups, with the former receiving near-real-time GEARS score predictions generated by a regression-based machine learning model. While both groups improved in technical metrics such as force application and tool acceleration, the feedback group showed increased awareness of their performance gaps, suggesting that automated feedback may enhance reflective learning even if it does not immediately accelerate early psychomotor development.

Table 2 Studies on surgical skill assessment & workflow analysis

Study	Methodology/Algorithm	Modalities
(Egert *et al.* 2020)	AI/ML (e.g., Computer Vision, ANN)	Instrument motion, eye tracking, force sensors, video
(Lyman *et al.* 2021)	CUSUM + ML (using ORI)	Kinematics (dVLogger from da Vinci system)
(Brown and Kuchenbecker 2023)	Automated GEARS-based scoring	Robotic instrument motion data (Smart Task Board)
(Hashemi *et al.* 2023)	AI-ready data acquisition framework	Video, 3D movement, event data
(Shafiei *et al.* 2023a)	GB	Eye gaze data
(Shafiei *et al.* 2023b)	GB, RF, MLR	EEG and eye gaze data
(Shafiei *et al.* 2024a)	XGBoost	EEG and eye-tracking (gaze, pupil, connectivity metrics)
(Shafiei *et al.* 2024b)	GB, RF	EEG and eye-tracking during VUA
(Takács *et al.* 2024)	Exploratory ML + statistical correlation analysis	Heart rate variability, posture, hand motion sensors (digital wearables)
(Hatcher *et al.* 2025)	Review of frameworks and assessments	Simulation tools, assessment checklists

Abbreviations: AI/ML, Artificial Intelligence / Machine Learning; ANN, Artificial Neural Network; CUSUM, Cumulative Sum Control Chart; dVLogger, da Vinci Logger; EEG, Electroencephalogram; GB, Gradient Boosting; GEARS, Global Evaluative Assessment of Robotic Skills; ML, Machine Learning; MLR, Multinomial Linear Regression; ORI, Operative Robotic Index; RF, Random Forest; VUA, Vesicourethral Anastomosis; XGBoost, Extreme Gradient Boosting.

Skill progression over time was the focus of a study (Lyman *et al.* 2021) that investigated the learning curve of novice surgeons performing hepaticojejunostomy using the da Vinci Surgical System. Kinematic data, including camera adjustments and tool movements, were recorded and analyzed with machine learning and stepwise "combination of an objective cumulative sum" (CUSUM) techniques. A new composite score, the Operative Robotic Index (ORI), was introduced to summarize performance across key metrics. The ORI effectively differentiated novice from intermediate skill levels and aligned closely with traditional CUSUM evaluations. These findings highlight how detailed kinematic tracking, and statistical modeling can be used to monitor skill development over time.

The evolution of robotic simulation education was the subject of a recent review (Hatcher *et al.* 2025) that emphasized the growing need for standardized training curricula tailored to RAS platforms like the da Vinci Xi. While early efforts such as the Fundamentals of Robotic Surgery program provide a baseline, more comprehensive tools and frameworks, such as GEARS, R-OSATS, and RO-SCORE, are needed to assess advanced robotic surgical skills. The authors also anticipate a future where emerging technologies such as AI, virtual reality, and AR are fully integrated into training platforms, making the da Vinci system a key player in next-generation surgical education.

Collectively, these studies illustrate the powerful role of the da Vinci Surgical System as both a surgical and educational platform. By capturing high-resolution data streams and integrating physiological, visual, and motion-based metrics, the system supports the development of automated models that can objectively assess skill levels, monitor stress responses, and improve training outcomes. These capabilities contribute to a future where surgical education is more standardized, feedback is more immediate and objective, and patient outcomes are continuously enhanced through data-driven learning.

Challenges in Adapting Deep Learning to Robot-Assisted Surgery

Despite rapid progress in applying DL and other machine learning methods to RAS, significant barriers remain before these techniques can be seamlessly adopted in real operating rooms. This section distills key challenges around data infrastructure, real-time performance, algorithm generalizability, interpretability, workflow integration, and regulatory/ethical concerns.

Data Availability, Quality, and Standardization: A fundamental challenge is assembling high-quality, large-scale datasets of robot-assisted procedures. The da Vinci Surgical System can record textual, kinematic, and video data, but there is no single, standardized protocol across institutions (Hashemi *et al.* 2023). In some contexts, researchers gather adverse event reports (Li *et al.* 2024) or produce specialized datasets for skill assessment (Lyman *et al.* 2021), but these remain fragmented. Meanwhile, anonymization requirements and the labor-intensive nature of manual annotation, particularly in advanced tasks like EEG- and eye-gaze–based skill assessment (Shafiei *et al.* 2023a,b, 2024b), discourage broad data-sharing. Even successful attempts to fuse multiple data modalities (e.g., vision, kinematics, and textual records) can be hampered by incompatible data formats, sensor noise, or incomplete metadata (Wu *et al.* 2020). The net effect is that many DL models are trained on small, nonrepresentative samples, limiting generalizability.

Real-Time Performance and Resource Constraints: DL algorithms used for tasks such as AR overlays, surgical-phase detection, or skill evaluation must produce sub-second updates. For instance, sensorless haptic feedback systems (Yilmaz *et al.* 2024) or real-time stress measurement (Takács *et al.* 2024) require tight latency

bounds for closed-loop control. Yet many robotics labs still rely on external graphics processing units or slower CPUs not specifically tuned to handle real-time inference. Even modest delays can disrupt surgical flow. Moreover, models of this class, such as the deep-transformer pipeline "Bert-BiLSTM" used for adverse-event classification (Li *et al.* 2024), typically require considerable compute resources. Balancing model complexity with real-time feasibility is an ongoing struggle.

Transfer Learning and Algorithm Generalizability: Neural networks often degrade when applied to new surgical environments, different endoscopic hardware, or novel tissue types (Egert *et al.* 2020; Hatcher *et al.* 2025). Similarly, skill classifiers that excel in simulator tasks (Rivero-Moreno *et al.* 2023) may stumble in real-world surgery with unfamiliar lighting conditions or tool usage patterns. Bridging simulation to reality remains a major hurdle. For instance, the realism of biomechanical simulations was improved by integrating real vision and kinematics data (Wu *et al.* 2020), although differences between controlled phantom data and anatomical variance in patients still limit direct transfer. Approaches to domain adaptation (ranging from augmented training sets to semi-supervised learning) are essential if we want robust models that generalize well across procedures and platforms.

Interpretability and Surgeon Acceptance: Black-box deep models trained on massive data can be difficult to interpret, thereby reducing surgeon trust. The necessity of transparent and easily digestible metrics for surgical performance has been emphasized in prior work (Egert *et al.* 2020). Similarly, it has been shown that while EEG or eye-tracking data can accurately gauge skill level, explaining why a model produces a particular skill rating remains challenging (Shafiei *et al.* 2023a,b, 2024b). Surgeons or medical trainees often rely on step-by-step guidance and immediate feedback; purely numerical or "black-box" predictions might be undervalued if they cannot be explained in a clinically meaningful manner. Fostering trust may require "explainable AI" methods (Setchi *et al.* 2020) to highlight relevant video frames, tissue edges, or motion trajectories that drive each inference.

Workflow Integration and Educational Gaps: Even when DL outputs are accurate, they can disrupt the robotic workflow if delivered through clunky interfaces or if they add cognitive load. Objective skill metrics such as the dVLogger-based ORI are presently reviewed post-hoc (Lyman *et al.* 2021); if such feedback were ever pushed into real time, an unfiltered stream of notifications could overwhelm surgeons. Likewise, the "Bert-BiLSTM" classifier developed to label da Vinci adverse-event reports remains a bench prototype (Li *et al.* 2024), and its clinical deployment would require careful alert management. At the same time, most residency programmes still lack dedicated AI or data-science instruction, creating a literacy gap that slows adoption (Hatcher *et al.* 2025; Egert *et al.* 2020). Reviews consequently stress the need for intuitive user-interface design and formal curricula that teach clinicians how to interpret and respond to algorithmic recommendations (Rivero-Moreno *et al.* 2023). Without such human–machine-interface refinements, even high-performing models may remain sidelined.

Regulatory, Ethical, and Liability Considerations: Regulatory frameworks for AI-driven surgical systems are still evolving (Egert *et al.* 2020). Tools that automate or partially automate tasks such as trocar placement or tissue retraction face extra scrutiny, since errors can have severe ramifications (Attanasio *et al.* 2020). Liability is another gray area (Marcus *et al.* 2024): if a trained model or algorithm misclassifies an adverse event or suggests an ill-advised maneuver, it is unclear whether the responsibility lies with the surgeon, the device manufacturer, or the hospital system. Data privacy is yet another consideration particularly for advanced analytics involving EEG, eye-gaze, or physiologic signals (Hashemi *et al.* 2023; Shafiei *et al.* 2024b). Without robust, standardized governance, it is challenging to deploy advanced AI functionalities at scale.

Proposed Conceptual Framework for a Multi-Modal Surgical Decision Support System

In light of previous studies (as discussed in the Results section) that focused on isolated aspects of robotic surgery, this study proposes a conceptual framework (Figure 4) that integrates these components into a unified, closed-loop system. The need for such a framework arises from the growing complexity of robotic surgical procedures and the demand for real-time, comprehensive decision support that enhances both surgical performance and training.

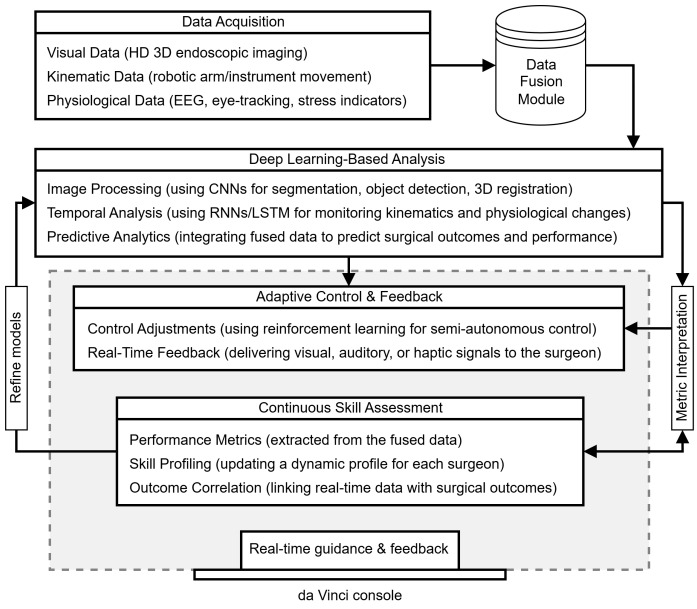

Figure 4 Proposed conceptual framework for the *da Vinci* system. This figure illustrates the interaction between the four core components: data acquisition and fusion, deep learning-based analysis, adaptive control and feedback, and continuous skill assessment. 3D, Three-Dimensional; CNN, Convolutional Neural Network; EEG, Electroencephalography; HD, High-Definition; LSTM, Long Short-Term Memory; RNN, Recurrent Neural Network.

Framework Components and Their Functions: The framework is composed of several interconnected components designed to capture, analyze, and act upon multi-modal data. Each component plays a vital role in ensuring that information is processed efficiently and utilized effectively to support surgical decision-making and continuous skill improvement.

The data acquisition and fusion component is critical for collecting and synchronizing diverse data sources to provide a comprehensive view of the surgical environment:

- **Visual Data:** HD 3D endoscopic imaging is captured by the da Vinci system. This data is used for AR overlays and real-time segmentation and registration of surgical sites.
- **Kinematic Data:** Detailed movement data from robotic arms and instruments, recorded via tools such as the dVLogger,

provides insights into instrument trajectories and motion patterns.
- **Physiological Data:** Wearable sensors collect metrics such as EEG, eye-tracking information, and stress indicators. This information reflects the surgeon's cognitive and emotional state during procedures.
- **Fusion Mechanism:** A central data fusion module synchronizes these diverse data streams into a unified dataset, ensuring that all modalities contribute to real-time analysis.

The deep learning-based analysis component leverages advanced DL models to interpret the fused data and extract actionable insights:

- **Image Processing:** CNNs are used to process visual data. These networks perform tasks such as object detection, segmentation, and 3D model alignment, thereby enhancing the visual context provided to the surgeon.
- **Temporal Analysis:** Recurrent neural network- or LSTM-based models analyze the kinematic and physiological data over time. This analysis supports dynamic skill assessment and monitors the surgeon's state throughout the procedure.
- **Predictive Analytics:** Machine learning algorithms integrate the fused data to predict surgical outcomes, provide alerts, and recommend adjustments based on historical performance and real-time trends.

The adaptive control and feedback component enables the system to dynamically adjust surgical parameters and provide real-time guidance based on continuous data analysis:

- **Control Adjustments:** Reinforcement learning algorithms enable the system to make semi-autonomous control adjustments. These adjustments can optimize instrument movements and camera positioning during surgery.
- **Real-Time Feedback:** The framework provides continuous feedback to the surgeon via the da Vinci console. This feedback may be visual, auditory, or haptic in nature, ensuring that the surgeon is informed of any deviations or potential improvements. Additionally, model interpretation (MI), such as through Shapley value-based approaches (Dean Pelegrina and Siraj 2024), helps the system deliver intelligible feedback (e.g., highlighting why a control adjustment is recommended).

The continuous skill assessment component focuses on evaluating and tracking surgeon performance over time to support targeted training and improved outcomes:

- **Performance Metrics:** Automated performance metrics are extracted from the fused data, allowing for an objective evaluation of surgical proficiency.
- **Skill Profiling:** This component continuously updates a skill profile for each surgeon. The profile is used to identify strengths, weaknesses, and trends in performance, which in turn supports targeted training interventions.
- **Outcome Correlation:** The framework correlates real-time performance data with surgical outcomes, contributing to a feedback loop that helps refine both the control system and the training protocols. Additionally, MI helps visually and numerically explain how specific data (e.g., instrument trajectories, EEG patterns) influence performance assessments. The two-sided connection provides an adaptive relationship between the component and MI (e.g., emphasizing temporal motion irregularities if fine motor control is a known issue). This transparency enables surgeons and educators to digest complex analytics in an intuitive and actionable manner.

Interactions Between Components: The proposed framework functions as an interconnected system in which each component reinforces and informs the others. In this system, the data acquisition module collects multi-modal information (including visual, kinematic, and physiological data) and feeds it into the DL-based analysis module, which interprets these data and subsequently informs the adaptive control system that provides real-time feedback to the surgeon. Meanwhile, the continuous skill assessment module monitors performance metrics and updates the surgeon's skill profile, which in turn is used to refine control strategies and training protocols. By integrating these diverse data streams into a unified framework, this approach bridges gaps observed in previous research, enhancing intraoperative decision-making and fostering a continuous learning environment that ultimately improves surgical outcomes and training efficiency. Additionally, the system integrates MI-based explanations that help visualize how specific inputs influence assessment outcomes. These explanations support clearer decision-making, promote user understanding of AI-driven suggestions, and contribute to more informed adjustments during both training and live procedures.

CONCLUSION

This study systematically reviewed recent advances in integrating DL with the da Vinci Surgical System, highlighting key innovations in autonomous instrument control, real-time image-guided navigation, skill assessment, and sensorless haptic feedback. These developments show great promise, yet challenges persist in data standardization, real-time performance, domain adaptation, and model interpretability. To address these challenges, the review organized recent DL applications into a comprehensive conceptual framework that supports real-time feedback, adaptive control, and continuous skill assessment, providing a foundation for future development and validation in RAS. As DL advances alongside sensing technologies, user-interface research, and evolving regulatory guidance, the framework can steer innovation toward safer, more autonomous, and intelligent surgical systems that improve both clinical practice and surgical education.

Although this preliminary framework is an important step toward a multi-modal DSS for RAS, further research and rigorous validation remain essential to assess real-world feasibility, optimize each component, and fully unlock the benefits of this integrated approach. The included studies vary methodologically, and many were conducted in simulated or controlled settings rather than operating rooms. Future work should prioritize clinical validation through well-designed prospective trials and enhance model transparency to foster surgeon trust and ensure robustness under real-world conditions. Ongoing updates to the da Vinci platform must be tracked to keep the framework compatible and clinically relevant. Progress will require close collaboration among engineers, surgeons, data scientists, and regulators to translate laboratory prototypes into safe, widely adopted clinical tools.

Acknowledgments

This study received no funding, grants, or other external support. An abstract based on the literature review component of this study was presented as an oral presentation at the 2nd *Biyobilim Buluşmaları*, held on April 17–18, 2025.

Availability of data and material

The analyses presented in this study are based on previously published literature, all of which is fully cited within the article. No new datasets were generated or used.

Conflicts of interest

The author declares that there is no conflict of interest regarding the publication of this paper.

Ethical standard

The author has no relevant financial or non-financial interests to disclose. This study did not involve human participants or animal experimentation.

LITERATURE CITED

Amparore, D., M. Sica, P. Verri, F. Piramide, E. Checcucci, *et al.*, 2024 Computer Vision and Machine-Learning Techniques for Automatic 3D Virtual Images Overlapping During Augmented Reality Guided Robotic Partial Nephrectomy. Technology in Cancer Research & Treatment **23**: 15330338241229368.

Attanasio, A., B. Scaglioni, M. Leonetti, A. F. Frangi, W. Cross, *et al.*, 2020 Autonomous Tissue Retraction in Robotic Assisted Minimally Invasive Surgery – A Feasibility Study. IEEE Robotics and Automation Letters **5**: 6528–6535.

Azizian, M., M. Liu, I. Khalaji, J. Sorger, D. Oh, *et al.*, 2020 The da Vinci Surgical System. In *Handbook of Robotic and Image-Guided Surgery*, pp. 39–55, Elsevier.

Boal, M. W. E., D. Anastasiou, F. Tesfai, W. Ghamrawi, E. Mazomenos, *et al.*, 2024 Evaluation of objective tools and artificial intelligence in robotic surgery technical skills assessment: a systematic review. British Journal of Surgery **111**: znad331.

Brown, J. D. and K. J. Kuchenbecker, 2023 Effects of automated skill assessment on robotic surgery training. The International Journal of Medical Robotics and Computer Assisted Surgery **19**: e2492.

Cannizzaro, D., M. Scalise, C. Zancanella, S. Paulli, S. Peron, *et al.*, 2024 Comparative Evaluation of Major Robotic Systems in Microanastomosis Procedures: A Systematic Review of Current Capabilities and Future Potential. Brain Sciences **14**: 1235.

Celotto, F., N. Ramacciotti, A. Mangano, G. Danieli, F. Pinto, *et al.*, 2024 Da Vinci single-port robotic system current application and future perspective in general surgery: A scoping review. Surgical Endoscopy **38**: 4814–4830.

Cepolina, F. and R. P. Razzoli, 2022 An introductory review of robotically assisted surgical systems. The International Journal of Medical Robotics and Computer Assisted Surgery **18**: e2409.

Dean Pelegrina, G. and S. Siraj, 2024 Shapley Value-Based Approaches to Explain the Quality of Predictions by Classifiers. IEEE Transactions on Artificial Intelligence **5**: 4217–4231.

D'Ettorre, C., A. Mariani, A. Stilli, F. Rodriguez Y Baena, P. Valdastri, *et al.*, 2021 Accelerating Surgical Robotics Research: A Review of 10 Years With the da Vinci Research Kit. IEEE Robotics & Automation Magazine **28**: 56–78.

DiMaio, S., M. Hanuschik, and U. Kreaden, 2011 The da Vinci Surgical System. In *Surgical Robotics*, edited by J. Rosen, B. Hannaford, and R. M. Satava, pp. 199–217, Springer US, Boston, MA.

Egert, M., J. E. Steward, and C. P. Sundaram, 2020 Machine Learning and Artificial Intelligence in Surgical Fields. Indian Journal of Surgical Oncology **11**: 573–577.

Gonzalez, G. T., U. Kaur, M. Rahman, V. Venkatesh, N. Sanchez, *et al.*, 2021 From the Dexterous Surgical Skill to the Battlefield—A Robotics Exploratory Study. Military Medicine **186**: 288–294.

Hashemi, N., M. B. S. Svendsen, F. Bjerrum, S. Rasmussen, M. G. Tolsgaard, *et al.*, 2023 Acquisition and usage of robotic surgical data for machine learning analysis. Surgical Endoscopy **37**: 6588–6601.

Hatcher, A. J., B. T. Beneville, and M. M. Awad, 2025 The evolution of surgical skills simulation education: Robotic skills. Surgery **181**: 109173.

Huber, M., S. Ourselin, C. Bergeles, and T. Vercauteren, 2022 Deep homography estimation in dynamic surgical scenes for laparoscopic camera motion extraction. Computer Methods in Biomechanics and Biomedical Engineering: Imaging & Visualization **10**: 321–329.

Iftikhar, M., M. Saqib, M. Zareen, and H. Mumtaz, 2024 Artificial intelligence: revolutionizing robotic surgery: review. Annals of Medicine & Surgery **86**: 5401–5409.

Khan, A., H. Yang, D. R. S. Habib, D. Ali, and J. Y. Wu, 2025 Development of a machine learning-based tension measurement method in robotic surgery. Surgical Endoscopy .

Kinoshita, T., R. Sato, E. Akimoto, Y. Tanaka, T. Okayama, *et al.*, 2022 Reduction in postoperative complications by robotic surgery: a case–control study of robotic versus conventional laparoscopic surgery for gastric cancer. Surgical Endoscopy **36**: 1989–1998.

Knudsen, J. E., U. Ghaffar, R. Ma, and A. J. Hung, 2024 Clinical applications of artificial intelligence in robotic surgery. Journal of Robotic Surgery **18**: 102.

Koh, D. H., W. S. Jang, J. W. Park, W. S. Ham, W. K. Han, *et al.*, 2018 Efficacy and Safety of Robotic Procedures Performed Using the da Vinci Robotic Surgical System at a Single Institute in Korea: Experience with 10000 Cases. Yonsei Medical Journal **59**: 975.

Koukourikis, P. and K. H. Rha, 2021 Robotic surgical systems in urology: What is currently available? Investigative and Clinical Urology **62**: 14.

Li, J., X. Gong, P. Li, L. Xiao, X. Chang, *et al.*, 2022 Application of Da Vinci robotic surgery system in cervical cancer: A single institution experience of 557 cases. Asian Journal of Surgery **45**: 707–711.

Li, T., W. Zhu, W. Xia, L. Wang, W. Li, *et al.*, 2024 Research on adverse event classification algorithm of da Vinci surgical robot based on Bert-BiLSTM model. Frontiers in Computational Neuroscience **18**: 1476164.

Lyman, W. B., M. J. Passeri, K. Murphy, I. A. Siddiqui, A. S. Khan, *et al.*, 2021 An objective approach to evaluate novice robotic surgeons using a combination of kinematics and stepwise cumulative sum (CUSUM) analyses. Surgical Endoscopy **35**: 2765–2772.

Marcus, H. J., P. T. Ramirez, D. Z. Khan, H. Layard Horsfall, J. G. Hanrahan, *et al.*, 2024 The IDEAL framework for surgical robotics: development, comparative evaluation and long-term monitoring. Nature Medicine **30**: 61–75.

Page, M. J., J. E. McKenzie, P. M. Bossuyt, I. Boutron, T. C. Hoffmann, *et al.*, 2021 The PRISMA 2020 statement: an updated guideline for reporting systematic reviews. BMJ p. n71.

Panesar, S., Y. Cagle, D. Chander, J. Morey, J. Fernandez-Miranda, *et al.*, 2019 Artificial Intelligence and the Future of Surgical Robotics. Annals of Surgery **270**: 223–226.

Pugin, F., P. Bucher, and P. Morel, 2011 History of robotic surgery : From AESOP® and ZEUS® to da Vinci®. Journal of Visceral Surgery **148**: e3–e8.

Reddy, K., P. Gharde, H. Tayade, M. Patil, L. S. Reddy, *et al.*, 2023 Advancements in Robotic Surgery: A Comprehensive Overview of Current Utilizations and Upcoming Frontiers. Cureus .

Rivero-Moreno, Y., S. Echevarria, C. Vidal-Valderrama, L. Stefano-Pianetti, J. Cordova-Guilarte, *et al.*, 2023 Robotic Surgery: A Comprehensive Review of the Literature and Current Trends. Cureus .

Saman, A., 2024 Next-Gen Surgery: AI Robots Leading the Way in

Healthcare. Archives of Community Medicine and Public Health **10**: 013–017.
Setchi, R., M. B. Dehkordi, and J. S. Khan, 2020 Explainable Robotics in Human-Robot Interactions. Procedia Computer Science **176**: 3057–3066.
Shafiei, S. B., S. Shadpour, and J. L. Mohler, 2024a An Integrated Electroencephalography and Eye-Tracking Analysis Using eXtreme Gradient Boosting for Mental Workload Evaluation in Surgery. Human Factors: The Journal of the Human Factors and Ergonomics Society p. 00187208241285513.
Shafiei, S. B., S. Shadpour, J. L. Mohler, K. Attwood, Q. Liu, *et al.*, 2023a Developing Surgical Skill Level Classification Model Using Visual Metrics and a Gradient Boosting Algorithm. Annals of Surgery Open **4**: e292.
Shafiei, S. B., S. Shadpour, J. L. Mohler, P. Rashidi, M. S. Toussi, *et al.*, 2024b Prediction of Robotic Anastomosis Competency Evaluation (RACE) metrics during vesico-urethral anastomosis using electroencephalography, eye-tracking, and machine learning. Scientific Reports **14**: 14611.
Shafiei, S. B., S. Shadpour, J. L. Mohler, F. Sasangohar, C. Gutierrez, *et al.*, 2023b Surgical skill level classification model development using EEG and eye-gaze data and machine learning algorithms. Journal of Robotic Surgery **17**: 2963–2971.
Steffens, D., K. E. McBride, N. Hirst, M. J. Solomon, T. Anderson, *et al.*, 2023 Surgical outcomes and cost analysis of a multispecialty robotic-assisted surgery caseload in the Australian public health system. Journal of Robotic Surgery **17**: 2237–2245.
Takács, K., E. Lukács, R. Levendovics, D. Pekli, A. Szijártó, *et al.*, 2024 Assessment of Surgeons' Stress Levels with Digital Sensors during Robot-Assisted Surgery: An Experimental Study. Sensors **24**: 2915.
Ullah, Z., S. Roy, S. Muhammad, C. Yu, H. Huang, *et al.*, 2024 Fluorescence imaging-guided surgery: current status and future directions. Biomaterials Science **12**: 3765–3804.
Wu, J. Y., P. Kazanzides, and M. Unberath, 2020 Leveraging vision and kinematics data to improve realism of biomechanic soft tissue simulation for robotic surgery. International Journal of Computer Assisted Radiology and Surgery **15**: 811–818.
Yilmaz, N., B. Burkhart, A. Deguet, P. Kazanzides, and U. Tumerdem, 2024 Enhancing robotic telesurgery with sensorless haptic feedback. International Journal of Computer Assisted Radiology and Surgery **19**: 1147–1155.

How to cite this article: Özcan, H. Deep Learning in Robot-Assisted Surgery: A Conceptual Framework for the da Vinci System. *Computers and Electronics in Medicine*, 2(2), 26-35, 2025.

ADBA
Computers and Electronics in Medicine
Cutting-Edge Scientific Solutions

e-ISSN: 3023-8609
RESEARCH ARTICLE
Vol.2 / No.2 / 2025 / pp.36-42
https://doi.org/10.69882/adba.cem.2025072

A Modified Transmission Line Modelling Approach for Bioheat Transfer

Burak Arıcıoğlu *,α,1 **and Abdullah Ferikoğlu** *,2

*Faculty of Technology, Electrical-Electronics Engineering, Sakarya University of Applied Sciences, Serdivan, Türkiye, αBiomedical Technologies Application and Research Center (Biyotam), Sakarya University of Applied Sciences, Serdivan, Türkiye.

ABSTRACT This study presents a modified Transmission Line Modelling (TLM) method for simulating bioheat transfer in biological tissues, with a particular focus on accounting for non-unidirectional blood flow. While the Pennes bioheat equation has been widely used for such problems, it assumes unidirectional perfusion and may overlook important thermal effects introduced by non-unidirectional blood flow. To address this limitation, a TLM-based formulation of the Klinger bioheat equation known for incorporating flow directionality is developed and implemented for one-dimensional (1D) problems. A novel TLM cell model is introduced to represent the governing equation and its associated boundary conditions. Validation is performed through a 1D multilayer human tissue model exposed to electromagnetic (EM) fields at multiple 4G carrier frequencies. Comparative results with the Finite Element Method (FEM) show strong agreement, especially under steady-state conditions. Furthermore, the proposed model reveals that the impact of non-unidirectional blood flow becomes more pronounced in thicker tissue layers, confirming the importance of incorporating convective terms. This work demonstrates that the modified TLM approach provides a stable, efficient, and more physiologically accurate method for bioheat simulations.

KEYWORDS
TLM
Bioheat transfer
Klinger bioheat equation
Pennes bioheat equation

INTRODUCTION

Bioheat transfer plays a critical role in understanding thermal interactions within biological tissues (Singh 2024; Ostadhossein and Hoseinzadeh 2024), with wide-ranging applications in medical diagnostics (D'Alessandro *et al.* 2024; Akulova and Sheremet 2024), hyperthermia-based therapies (Jiang 2024; Sherief *et al.* 2024), and cryosurgery studies (Barman *et al.* 2021; Kumar and Rai 2022) among others. Traditional models, such as Pennes' bioheat equation (Pennes 1948), have provided a foundational framework for analysing heat conduction in perfused tissues. However, these models often assume simplified blood flow patterns, typically unidirectional and spatially averaged perfusion, which may not adequately capture the complexity of heat transmission in biological tissues (Hristov 2019; Tucci *et al.* 2021).

The Transmission Line Modelling (TLM) method has gained attention in the literature as a robust numerical technique for solving the wave equation, the diffusion equation and the linear combination of both wave and diffusion types of partial differential equations (PDEs) (Christopoulos and Christopoulos 1995; Aricioglu and Ferikoglu 2021; Johns 1977). A key advantage of the TLM method lies in its unconditional stability and the fact that it does not require matrix inversion for time-domain solutions, making it both efficient and scalable for large and complex simulations (Milan and Gebremedhin 2018).

In this study, a modified TLM method is presented for simulating bioheat transfer, extending the classical framework by incorporating non-unidirectional blood flow effects. The Pennes bioheat equation is one of the most commonly used models in the literature for solving bioheat transfer problems (Ostadhossein and Hoseinzadeh 2022; Abro *et al.* 2021; El-Sapa *et al.* 2024; Ezzat *et al.* 2014; Ferras *et al.* 2015). However, as noted by H.G. Klinger, the Pennes equation neglects the effects of non-unidirectional blood flow, which may lead to inaccuracies (Klinger 1974). Therefore, this study employs the Klinger bioheat equation as an alternative. To implement this, a new TLM cell model was developed that accounts for non-unidirectional blood flow. To the best of the author's knowledge, there is currently no TLM-based implementation of the Klinger bioheat equation in the literature. Thus, the TLM model for the Klinger equation constitutes the novel contribution of this work. For simplicity, only the one-dimensional (1D) case is considered.

The remainder of the paper is organized as follows: Section 2 presents the materials and methods. Section 3 provides numerical simulations and results. Finally, Section 4 concludes the paper with a summary of findings and perspectives for future work.

MATERIALS AND METHODS

In this section, the application of the TLM method to 1D bioheat problems is explained. The TLM method can be used to solve wave equations, diffusion equations, or any combination of the two. The general thermal diffusion equation is:

Manuscript received: 15 April 2025,
Revised: 24 May 2025,
Accepted: 5 July 2025.

[1]baricioglu@subu.edu.tr (**Corresponding author**)
[2]af@subu.edu.tr

$$k\nabla^2 T = \rho C \frac{\partial T}{\partial t} - Q. \tag{1}$$

Here, k is the thermal conductivity (W/mK), T is the temperature (K), ρ is the density (kg/m^3), C is the specific heat capacity (J/kgK), and Q is the heat source term (W/m^3). In biological tissues, thermal diffusion described by the Pennes bioheat equation is given by (Pennes 1948)

$$k_T\nabla^2 T = \rho_T C_T \frac{\partial T}{\partial t} + \omega_b C_b (T - T_b) - Q_{\text{met}} - Q_e. \tag{2}$$

Here, k_T is the thermal conductivity of the tissue (W/m·K), T is the temperature (K), ρ_T is the tissue density (kg/m^3), C_T is the specific heat capacity of the tissue (J/kg·K), ω_b is the blood perfusion rate (kg/m^{3}s), C_b is the specific heat capacity of blood (J/kg·K), T_b is the initial temperature of blood (K), Q_met is the metabolic heat generation rate (W/m^3), and Q_e is the power absorbed by the tissue from an external heat source (W/m^3). The Klinger bioheat equation is (Klinger 1974):

$$k_T\nabla^2 T = \rho_T C_T \frac{\partial T}{\partial t} + (\rho_T C_T)(\vec{u}\cdot\nabla T) - Q_{\text{met}} - Q_e. \tag{3}$$

The term $(\rho_T C_T)(\vec{u}\cdot\nabla T)$ represents the effect of blood flow velocity on heat distribution within the tissue, where $\vec{u}$ is the velocity vector (m/s). In this model, the physical properties of the tissue are assumed to be constant, and the blood flow is considered as an incompressible.

The new transmission line model for Klinger bioheat equation

The 1D transmission line that models the Klinger bioheat equation is shown in Figure 1

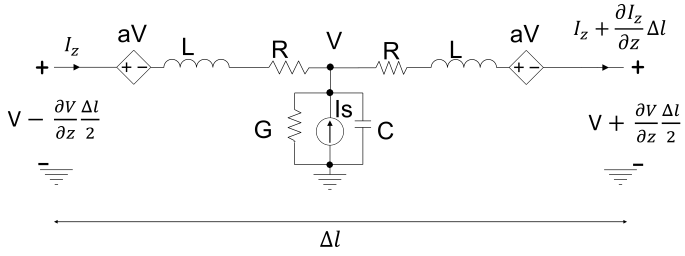

Figure 1 The 1D TLM circuit for the Klinger bioheat model.

In Figure 1, the current source models the metabolic and other heat sources (Milan and Gebremedhin 2018; Desai *et al.* 1992; Milan *et al.* 2014; Milan and Gebremedhin 2016), while the voltage-controlled voltage source represents the effect of blood flow on the bioheat distribution. Applying the Kirchhoff's Voltage Law (KVL) to the circuit in Figure 1 yields.

$$V - \frac{\partial V}{\partial z}\frac{\Delta l}{2} - aV - L\frac{\Delta l}{2}\frac{\partial I_z}{\partial t} - R\frac{\Delta l}{2}I_z - V = 0. \tag{4}$$

If (4) is rearranged and both sides of the equation are divided by $\Delta l/2$, then the following is obtained

$$-\frac{\partial V}{\partial z} - \frac{2a}{\Delta l}V = L\frac{\partial I_Z}{\partial t} + RI_Z. \tag{5}$$

Applying Kirchhoff's Current Law (KCL) at node V in Figure 1 gives:

$$I_Z - \left(I_Z + \frac{\partial I_Z}{\partial z}\frac{\Delta l}{2}\right) - \left(G\frac{\Delta l}{2}V + C\frac{\Delta l}{2}\frac{\partial V}{\partial t} - I_S\right) = 0. \tag{6}$$

If (6) is rearranged and both sides are divided by $\frac{\Delta l}{2}$ yields:

$$\frac{\partial I_Z}{\partial z} = -GV - C\frac{\partial V}{\partial t} + \frac{2I_S}{\Delta l}. \tag{7}$$

Taking the derivative of (5) with respect to z, and the derivative of (7) with respect to t, then combining the two yields:

$$\frac{\partial^2 V}{\partial z^2} = LC\frac{\partial^2 V}{\partial t^2} + (LG + RC)\frac{\partial V}{\partial t} + RGV + \frac{2a}{\Delta l}\frac{\partial V}{\partial z} - \frac{L}{\Delta l}\frac{\partial I_S}{\partial t} - \frac{RI_S}{\Delta l}. \tag{8}$$

(8) contains both wave and diffusion terms. Since the bioheat equation is fundamentally a diffusion equation, the diffusion terms should dominate. This is ensured by the condition: $LG + RC \gg \omega LC$ where R, L, G, and C denote the resistance, inductance, conductivity, and capacitance per unit length of the transmission line, and ω is the angular frequency. A simple way to satisfy this condition is by setting $L = 0$, which eliminates the wave term in (8). When $L = 0$, (8) simplifies to:

$$\frac{\partial^2 V}{\partial z^2} = RC\frac{\partial V}{\partial t} + RGV + \frac{2a}{\Delta l}\frac{\partial V}{\partial z} - \frac{RI_S}{\Delta l}. \tag{9}$$

By comparing (3) with (9), the equivalence relations shown in Table 1 can be established.

For the transmission line shown in Figure 1, the resistance R is selected as $1/k_T$. The remaining lumped parameters are then calculated accordingly, based on this choice. The corresponding values of the lumped elements for the 1D transmission line, expressed in terms of the tissue's thermal properties, are summarized in Table 2.

Boundary Condition Models in the TLM Used for Bioheat Problems

Heat transfer problems, including those involving bioheat transfer, typically involve four types of boundary conditions: interface boundary conditions, Dirichlet boundary conditions, Neumann boundary conditions, and convection boundary conditions. For simplicity in modeling these conditions, the effect of blood flow velocity on heat transfer is neglected at the boundaries.

Interface Boundary Condition The interface boundary condition is used in structures composed of multiple different materials. For the interface boundary condition to be valid, the following two conditions must be satisfied:

- The surfaces of the two different materials in contact must be at the same temperature.
- The interface must not store any energy.

The interface boundary condition can be defined as in (10).

$$-k_{T1}\frac{\partial T_1}{\partial x} = -k_{T2}\frac{\partial T_2}{\partial x}. \tag{10}$$

Here, k_{T1} and k_{T2} represent the thermal conductivities of two different tissues, while T_1 and T_2 denote the temperature distributions in the two different tissues. This boundary condition demonstrates the applicability of the TLM method in solving bioheat transfer equations for heterogeneous media. When examining the equivalencies given in Table 2, it is observed that the inverse of thermal conductivity is the R parameter of the transmission line, while the voltage corresponds to temperature. Therefore, when applying (10), the interface boundary condition can be represented as shown in Figure 2.

In Figure 2, at the surface where the two tissues are in contact, i.e., where the transmission line models are connected, the voltages

Table 1 Equivalence between the 1D Transmission Line and Klinger Bioheat Equation.

1D Transmission Line	Klinger Bioheat Equation
V (V)	T (K)
RC (Ω·F/m^2)	$\frac{\rho_T C_T}{k_T}$ (J·kg/m^3)
$\frac{2a}{\Delta l}$ (1/m)	$\frac{\rho_T C_T \lvert\vec{u}\rvert}{k_T}$ (W/kg·m^2)
RG (1/m^2)	$\frac{\omega_b C_b}{k_T}$ (W/m^3·K)
$\frac{I_S R}{\Delta l}$ (V/m^2)	$\frac{\omega_b C_b T_b + Q_{\text{met}} + Q_e}{k_T}$ (K/m^2)

Table 2 Equivalence between 1D Transmission Line Lumped Parameters and Thermal Properties dependent Parameters of Tissue.

1D Transmission Line Lumped Parameters	Thermal Properties dependent Parameters of Tissue
R (Ω/m)	$\frac{1}{k_T}$ (K·m/W)
C (F/m)	$\rho_T C_T$ (J/m^3·K)
G (1/Ω/m)	$\omega_b C_b$ (W/m^3·K)
$2a$	$\frac{\rho_T C_T \lvert\vec{u}\rvert \Delta l}{k_T}$
I_S (A)	$(\omega_b C_b T_b + Q_{\text{met}} + Q_e)\Delta l$ (W/m^2)

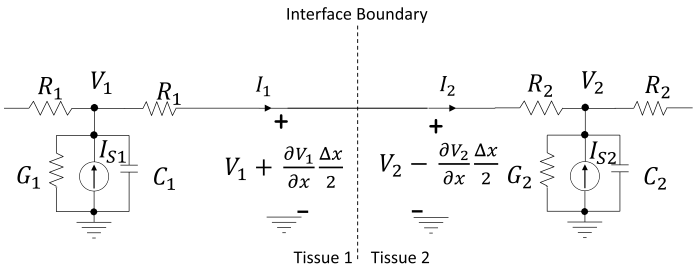

Figure 2 The circuit model for interface boundary condition in the TLM.

are equal, and there is no circuit element that stores energy at the interface. This satisfies the two conditions required for the interface boundary condition. The currents I_1 and I_2 in the figure are equal and can be calculated as in (11).

$$\begin{aligned} I_1 &= -\frac{1}{R_1}\frac{\partial V_1}{\partial x}, \\ I_2 &= -\frac{1}{R_2}\frac{\partial V_2}{\partial x}, \\ I_1 = I_2 &= -\frac{1}{R_1}\frac{\partial V_1}{\partial x} = -\frac{1}{R_2}\frac{\partial V_2}{\partial x}. \end{aligned} \tag{11}$$

Dirichlet Boundary Condition In heat transfer problems, the Dirichlet boundary condition indicates that the surface temperature remains constant. An example of this boundary condition occurs when the surface is in contact with a melting solid or a boiling liquid. In both cases, heat transfer occurs at the contact surface, but the surface temperature remains constant as the solid or liquid undergoes phase change.

In bioheat transfer problems, the Dirichlet boundary condition can be implemented in the TLM method by connecting a fixed voltage source at the end of the TLM cell to satisfies the Dirichlet condition. The modelling of this boundary condition is shown in Figure 3.

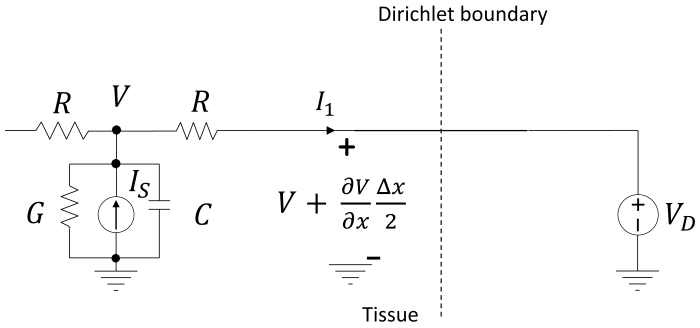

Figure 3 The circuit model for the Dirichlet boundary condition in the TLM.

Neumann Boundary Condition In heat transfer problems, the Neumann boundary condition is applied when the rate of temperature change, or the heat flux, at the boundary surface is known. This situation is mathematically expressed as in (12).

$$q_y = -k_T \frac{\partial T}{\partial x}. \tag{12}$$

Here, q_y is the heat flux at the boundary surface (W/m), and k_T is the thermal conductivity of the tissue (W/m·K). The Neumann boundary condition in the TLM model is shown in Figure 4.

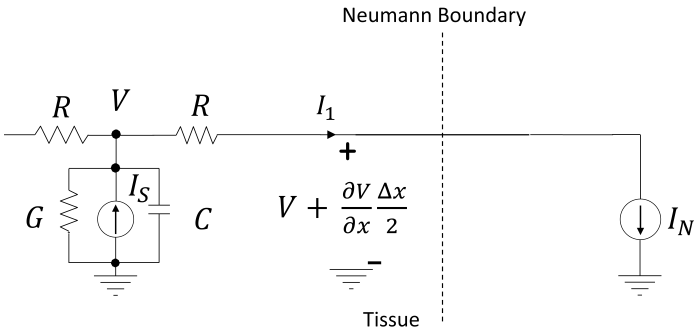

Figure 4 The circuit model for the Neumann boundary condition in the TLM.

In Figure 4, I_1 and I_N are equal, and can be calculated as follows:

$$I_1 = I_N = -\frac{1}{R}\frac{\partial V}{\partial x}. \tag{13}$$

In the Neumann boundary condition, the case where the heat flux at the boundary surface is zero is a special case and is also referred to as the insulated (adiabatic) boundary condition. This situation is mathematically expressed as in (14).

$$q_y = -k_T\frac{\partial T}{\partial x} = 0. \tag{14}$$

The adiabatic boundary condition in the TLM model is shown in Figure 5. In the figure, since the transmission line is terminated with an open circuit, the value of current I_1 is zero. Thus, the condition given in (14) is satisfied.

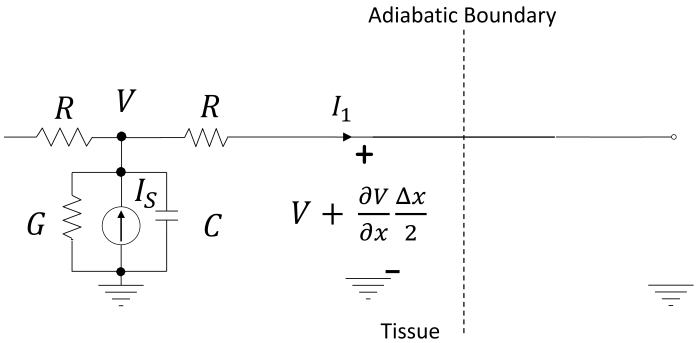

Figure 5 The circuit model for the adiabatic boundary condition in the TLM.

Convection Boundary Condition In heat transfer problems, the convection boundary condition is also known as Newton's boundary condition states that the heat transfer at the boundary surface is obtained from the conservation of energy at the surface. It is assumed that no energy is stored at the boundary surface. Therefore, the net heat flux entering the surface is equal to the net heat flux leaving the surface. Mathematically, the convection boundary condition is expressed as in (15).

$$-k_T\frac{\partial T}{\partial x} = h(T_T - T). \tag{15}$$

Here, k_T is the thermal conductivity of the tissue (W/m·K), T is the temperature in the tissue (K), h is the heat transfer coefficient at the boundary surface (W/m), and T_T is the temperature on the other side of the boundary surface. The model for the convection boundary condition is shown in Figure 6.

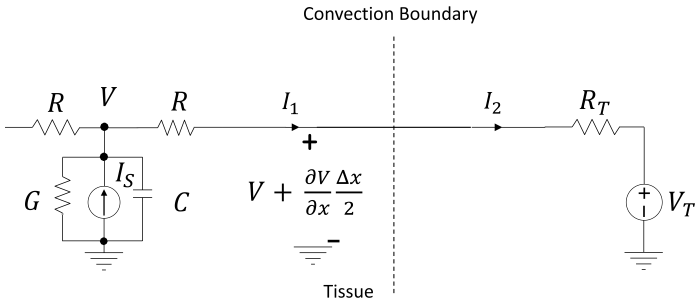

Figure 6 The circuit model for the convection boundary condition in the TLM model.

In Figure 6, the currents I_1 and I_2 are equal and can be written as follows.

$$\begin{aligned} I_1 &= -\frac{1}{R}\frac{\partial V}{\partial x}, \\ I_2 &\approx \frac{1}{R_T}(V - V_T), \\ I_1 &= I_2 = -\frac{1}{R}\frac{\partial V}{\partial x} = \frac{1}{R_T}(V - V_T). \end{aligned} \tag{16}$$

In Table 3, the modelling of boundary conditions of the heat transfer problems in TLM is summarized.

SIMULATIONS AND RESULTS

In the simulation a 1D bioelectromagnetic problem is considered. In the problem a 1D multilayer human body tissue model selected for the study. The multilayer human body tissue model used in this work is shown in Figure 7. The model consists of skin, fat, and muscle tissues, with thicknesses of 1 mm, 4 mm, and 10 mm, respectively (Lin 1986).

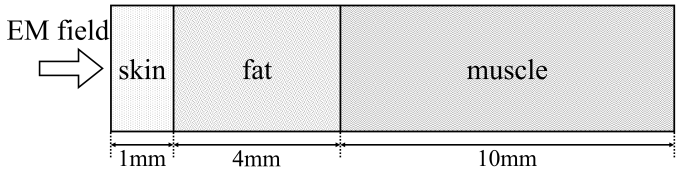

Figure 7 Multilayer human body tissue model.

In this section, the resulting temperature rise due to EM exposure in a one-dimensional (1D) multilayered human body tissue model were obtained using both the Transmission Line Modelling (TLM) method and the Finite Element Method (FEM). For the tissue model presented in Figure 7, the distribution of EM fields within the tissues was calculated at various 4G frequencies. The carrier frequencies considered were 700 MHz, 900 MHz, 1800 MHz, 2100 MHz, and 2600 MHz. The incident electric field intensity was

Table 3 The relationship between boundary conditions and the parameters of the TLM models.

	TLM	Heat Transfer Problem
Interface Boundary Condition	V_1	T_1
	V_2	T_2
	$1/R_1$	k_1
	$1/R_2$	k_2
Dirichlet Boundary Condition (Constant Surface Temperature)	V_D	T_D
Neumann Boundary Condition	I_N	q_y
Adiabatic Boundary Condition	Open Circuit	$q_y = 0$
Convection Boundary Condition	V_T	T_T
	$1/R_T$	h

set to 10 V/m for all 4G frequencies. This selected field intensity is below the general public exposure limits specified by the ICNIRP (International Commission on Non-Ionizing Radiation Protection) guidelines for all the given frequencies (ICNIRP 2009). The exposure duration used in the temperature rise calculations was set to 2 hours.

Figure 8 shows the simulation setup for the 1D bioelectromagnetic problem. In the figure, the lossy transmission lines labelled T_{Si}, T_{Fj}, and T_{Mk} represent the skin, fat, and muscle tissues, respectively. In the simulation, the skin tissue is divided into 10 equal segments, the fat tissue into 6 equal segments, and the muscle tissue into 4 equal segments. The lengths of the TLM cells representing the skin, fat, and muscle tissues are 0.1 mm, 0.67 mm, and 1 mm, respectively. The impedance, denoted as Z_L in the figure, is chosen to be as open circuit. In other words, the simulation is terminated with adiabatic boundary condition for simplicity.

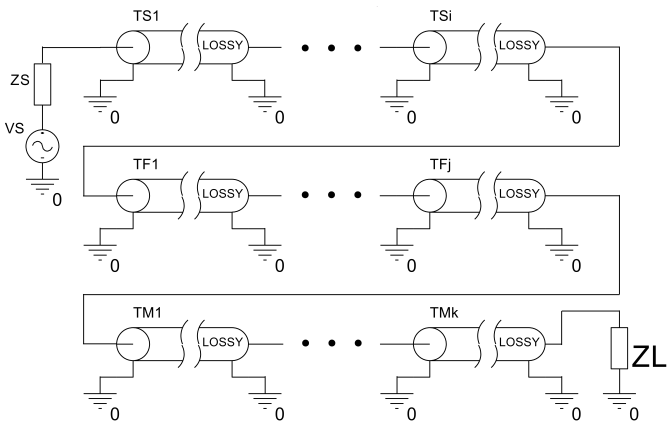

Figure 8 The simulation setup for the 1D bioelectromagnetic problem.

The average temperature rise in the body tissue model after 2 hours of exposure to the EM field is shown in Figure 9. In Figure 9, the temperature rise calculation is performed using both the TLM method and the FEM method. Additionally, the ambient temperature is chosen to be 25°C for the temperature rise calculations.

When the results of both methods are compared, the temperature rises obtained by both methods are quite similar. The total average temperature rise in the tissue model decreases monotonically with frequency at 4G frequencies. Even in the worst-case scenario, the total average temperature rise is less than 0.1°C ($\approx$ 0.07°C).

Figure 10 shows the temperature increases at both boundaries of the muscle tissue in the analyses conducted using the Klinger bioheat transfer equation-based FEM and TLM, the Pennes bioheat transfer equation-based TLM method at 2600 MHz. The muscle tissue was selected for this analysis because it is the thickest layer in the model.

As seen in Figure 10, the temperature increases at both boundaries of the muscle tissue appear to be very similar between the Klinger bioheat transfer equation-based TLM and the FEM method, particularly in the steady-state condition. The temperature difference at both and of the muscle tissue is about 1m°C. On the other hand, the results obtained using the Pennes bioheat transfer equation-based TLM show nearly identical temperature increases at both ends of the muscle tissue. This difference arises because the effect of blood flow velocity on temperature variation is neglected in the Pennes bioheat transfer equation. As a result, more accurate results were obtained using the newly developed Klinger bioheat transfer equation-based TLM.

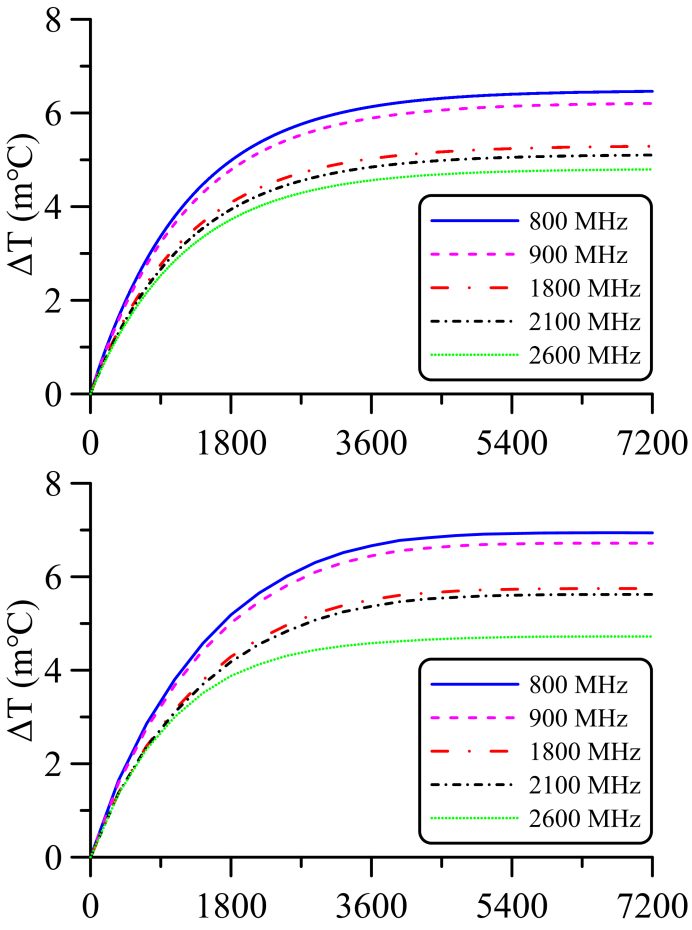

Figure 9 The average temperature rise due to exposure to 4G frequencies in a multilayered tissue model (top) TLM based method, (bottom) FEM based method.

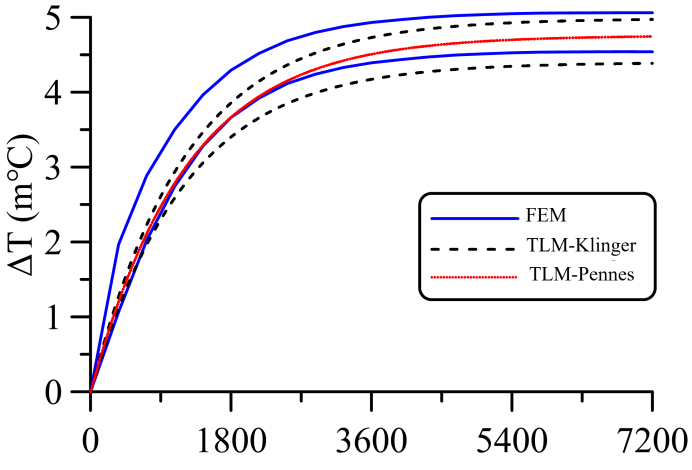

Figure 10 Temperature increases obtained at observations points in the muscle tissue using the Klinger and Pennes bioheat transfer equations-based FEM and the TLM method.

CONCLUSION

In this study, a modified Transmission Line Modelling (TLM) method was developed and applied to bioheat transfer problems by incorporating the effects of non-unidirectional blood flow through the Klinger bioheat equation. The method was validated through simulations of a multilayer human body tissue model exposed to 4G electromagnetic fields, with temperature rise predictions compared against those from the Finite Element Method (FEM). The results demonstrate strong agreement between the proposed TLM method and FEM, especially under steady-state conditions. While the Pennes-based TLM model showed nearly symmetric temperature distributions, the Klinger-based TLM method captured directional differences at tissue boundaries, underscoring the importance of modelling convective transport. The observed total average temperature rise remained below critical safety thresholds in all test cases, supporting compliance with ICNIRP exposure guidelines.

However, several limitations must be acknowledged. The assumption of homogeneous tissue properties simplifies the geometry and may not fully capture the complexities of real biological structures. Additionally, the model neglects temperature-dependent perfusion, which can influence thermal behavior in vivo. Despite these simplifications, the study lays important groundwork for extending TLM-based techniques to more anatomically realistic geometries and heterogeneous tissue conditions in future research. Overall, the Klinger-based TLM approach offers enhanced accuracy and flexibility for modelling complex bioheat transfer phenomena, particularly in scenarios where blood flow directionality plays a significant role.

Ethical standard

The authors have no relevant financial or non-financial interests to disclose.

Availability of data and material

Not applicable.

Conflicts of interest

The authors declare that there is no conflict of interest regarding the publication of this paper.

LITERATURE CITED

Abro, K. A., A. Atangana, and J. F. Gomez-Aguilar, 2021 An analytic study of bioheat transfer Pennes model via modern non-integers differential techniques. The European Physical Journal Plus **136**: 1–11.

Akulova, D. V., and M. A. Sheremet, 2024 Mathematical Simulation of Bio-Heat Transfer in Tissues Having Five Layers in the Presence of a Tumor Zone. Mathematics **12(5)**: 676.

Aricioglu, B., and A. Ferikoglu, 2021 Thermal Effects of 5G Frequency EM Waves on Ocular Tissue. The Applied Computational Electromagnetics Society Journal (ACES): 286–397.

Barman, C., P. Rath, and A. Bhattacharya, 2021 A non-Fourier bioheat transfer model for cryosurgery of tumor tissue with minimum collateral damage. Computer Methods and Programs in Biomedicine **200**: 105857.

Christopoulos, C., and C. Christopoulos, 1995 *The Transmission-line Modeling Method: TLM*. IEEE Press, New York, USA.

D'Alessandro, G., P. Tavakolian, and S. Sfarra, 2024 A review of techniques and bio-heat transfer models supporting infrared thermal imaging for diagnosis of malignancy. Applied Sciences **14(4)**: 1603.

Desai, R. A., A. J. Lowery, C. Christopoulos, P. Naylor, J. M. V. Blanshard, and K. Gregson, 1992 Computer modelling of microwave cooking using the transmission-line model. IEE Proceedings A (Science, Measurement and Technology) **139(1)**: 30–38.

El-Sapa, S., A. A. El-Bary, W. Albalawi, and H. M. Atef, 2024 Modelling Pennes', bioheat transfer equation in thermoelasticity with one relaxation time. Journal of Electromagnetic Waves and Applications **38(1)**: 105–121.

Ezzat, M. A., N. S. AlSowayan, Z. I. Al-Muhiameed, and S. M. Ezzat, 2014 Fractional modelling of Pennes' bioheat transfer equation. Heat and Mass Transfer **50**: 907–914.

Ferras, L. L., N. J. Ford, M. L. Morgado, J. M. Nobrega, and M. S. Rebelo, 2015 Fractional Pennes' bioheat equation: theoretical and numerical studies. Fractional Calculus and Applied Analysis **18**: 1080–1106.

Hristov, J., 2019 Bio-heat models revisited: concepts, derivations, nondimensalization and fractionalization approaches. Frontiers in Physics **7**: 189.

International Commission on Non-Ionizing Radiation Protection, 2009 ICNIRP statement on the Guidelines for limiting exposure to time-varying electric, magnetic, and electromagnetic fields (up to 300 GHz). Health Physics **97(3)**: 257–258.

Jiang, Q., 2024 Study of magnetic hyperthermia based cancer treatment using a holistic simulation framework.

Johns, P. B., 1977 Numerical modelling by the TLM method. In *Large Engineering Systems* (pp. 139–151), Pergamon.

Klinger, H. G., 1974 Heat transfer in perfused biological tissue-I: General theory. Bulletin of Mathematical Biology **36(4)**: 403–415.

Kumar, M., and K. N. Rai, 2022 Three phase bio-heat transfer model in three-dimensional space for multiprobe cryosurgery. Journal of Thermal Analysis and Calorimetry **147(24)**: 14491–14507.

Lin, J. C., 1986 Microwave propagation in biological dielectrics with application to cardiopulmonary interrogation. In *Medical Applications of Microwave Imaging* (pp. 47–58), IEEE Press.

Milan, H. F. M., and K. G. Gebremedhin, 2016 Solving bioenergetics problems with the transmission-line modeling (TLM) method. In *2016 ASABE Annual International Meeting*, (p. 1), American Society of Agricultural and Biological Engineers.

Milan, H. F., and K. G. Gebremedhin, 2018 General node for transmission-line modeling (TLM) method applied to bio-heat transfer. International Journal of Numerical Modelling: Electronic Networks, Devices and Fields **31(5)**.

Milan, H. F., C. A. Carvalho Jr., A. S. Maia, and K. G. Gebremedhin, 2014 Graded meshes in bio-thermal problems with transmission-line modeling method. Journal of Thermal Biology **45**: 43–53.

Ostadhossein, R., and S. Hoseinzadeh, 2022 The solution of Pennes' bio-heat equation with a convection term and nonlinear specific heat capacity using Adomian decomposition. Journal of Thermal Analysis and Calorimetry **147(22)**: 12739–12747.

Ostadhossein, R., and S. Hoseinzadeh, 2024 Developing computational methods of heat flow using bioheat equation enhancing skin thermal modeling efficiency. International Journal of Numerical Methods for Heat & Fluid Flow **34(3)**: 1380–1398.

Pennes, H. H., 1948 Analysis of tissue and arterial blood temperatures in the resting human forearm. Journal of Applied Physiology **1(2)**: 93–122.

Sherief, H. H., M. F. Zaky, M. F. Abbas, and S. A. Mahrous, 2024 Mathematical modeling of heat transfer in tissues with skin tumor during thermotherapy. PLOS One **19(5)**: e0298256.

Singh, M., 2024 Modified Pennes bioheat equation with heterogeneous blood perfusion: A newer perspective. International Journal of Heat and Mass Transfer **218**: 124698.

Tucci, C., M. Trujillo, E. Berjano, M. Iasiello, A. Andreozzi, and G. P. Vanoli, 2021 Pennes' bioheat equation vs. porous media approach in computer modeling of radiofrequency tumor ablation. Scientific Reports **11(1)**: 5272.

How to cite this article: Arıcıoğlu, B. and Ferikoğlu, A. A Modified Transmission Line Modelling Approach for Bioheat Transfer. *Computers and Electronics in Medicine*, 2(2), 36-42, 2025.

ADBA
Computers and Electronics in Medicine
Cutting-Edge Scientific Solutions

e-ISSN: 3023-8609
RESEARCH ARTICLE
Vol.2 / No.2 / 2025 / pp.43-52
https://doi.org/10.69882/adba.cem.2025073

AI-Driven Classification of Anemia and Blood Disorders Using Machine Learning Models

Yigitcan Cakmak *,1 **and Ishak Pacal** α,2
*Department of Computer Engineering, Faculty of Engineering, Igdir University, 76000, Igdir, Türkiye.

ABSTRACT

Anemia and other blood disorders are serious global health issues affecting millions of individuals. These conditions, often triggered by insufficient hemoglobin or red blood cells, can manifest symptoms like fatigue, weakness, and reduced immune function. When such disorders progress into advanced stages, they can compromise organ function and overall quality of life, making early diagnosis especially critical. In recent years, as the value of prompt detection has become increasingly clear, artificial intelligence and autonomous diagnostic technologies have begun to take center stage in the medical community. Machine learning models excel at parsing complex datasets and generating accurate, rapid assessments, thus offering clinicians robust decision-support tools. Through these AI-driven methods, healthcare professionals can better interpret patients' blood metrics and clinical indicators, enabling them to identify diseases at earlier stages and develop more effective treatment strategies. This study proposes a machine learning–based approach to classify various types of anemia and related blood disorders, including iron deficiency anemia, leukemia, and thrombocytopenia. We trained five contemporary algorithms Decision Tree, Random Forest, CatBoost, Gradient Boosting, and XGBoost using critical blood parameters such as white and red blood cell counts, hemoglobin levels, and platelet counts. Notably, Gradient Boosting emerged as the most accurate model, achieving an impressive 99.19% accuracy rate. These findings underscore how AI-powered autonomous diagnostic systems have the potential to revolutionize hematology by facilitating earlier and more precise disease detection.

KEYWORDS
Anemia
Machine learning
Blood disorders
Clinical decision support
Hematological data

INTRODUCTION

Anemia, a spectrum of blood orders characterized by the shortness of red blood cells or hemoglobin, is one of the most common global health challenges that considerably threatens people of all ages. While the symptoms differ, common manifestations of anemia are fatigue, weakness, and pale skin (Yoshida 2024). Causes found in the medical literature about anemia include nutritional deficiencies, chronic diseases, or diseases associated with the bone marrow (Krieg *et al.* 2024). Early identification of anemia is very critical for proper treatment and management because untreated anemia may develop into other life-threatening conditions. The classification of anemia and other blood ailments like leukemia, thrombocytopenia, and macrocytic anemia is very important when it comes to the diagnostic aspect and to plan for treatment (Fentie *et al.* 2020; Subba and Araveti 2025).

Identification of anemia falls along the lines of multiple contributors called blood markers at very different levels; the most critical among them are white blood cell count (WBC), red blood cell count (RBC), hemoglobin (HGB), and platelet count (PLT) (Karra *et al.* 2025; Malak *et al.* 2025; Li *et al.* 2025). Recent advancements in machine learning (ML) include various algorithms such as Decision Tree (DT), Random Forest (RF), CatBoost, Gradient Boosting (GB), and XGBoost, showing great potential in the classification and prediction of blood disorders; in our case, anemia. Traditional methods for diagnosis tend to take longer and are expensive, whereas ML algorithms have the capability of analyzing medical data that is very complicated and involved, very quickly and accurately (Link *et al.* 2024).

Integration of the algorithms of Decision Tree (DT), Random Forest (RF), CatBoost, Gradient Boosting (GB), and XGBoost highly improved the accuracy of the disease classification models. For our study, we examined the algorithms in classifying various types of anemia and other blood disorders; the Gradient Boosting algorithm recorded the highest accuracy at 99.19%, while Decision Tree trailed by achieving 98.38%. CatBoost and XGBoost achieved accuracy levels of 97.98% each, and Random Forest achieved satisfactory accuracy at 96.76%. Therefore, our results prove that, in the medical field, claims made about the efficiency of using 'ML' algorithms in the proper classification of blood disorders are hugely encouraging for early diagnosis and timely interventional treatment (Ramzan *et al.* 2024; Kitaw *et al.* 2024).

Machine learning and deep learning has revolutionized healthcare by offering solutions that help make diagnosis and treatment more efficient (Pacal 2024b; Pacal and Attallah 2025a; Aruk *et al.* 2025; İnce *et al.* 2025; Ince *et al.* 2025). The use of ML models concerning blood disorder classification is an important step into more

Manuscript received: 21 March 2025,
Revised: 5 July 2025,
Accepted: 9 July 2025.

[1]ygtcncakmak@gmail.com (**Corresponding author**)
[2]ishak.pacal@igdir.edu.tr

personalized medicine; algorithms can identify subtle patterns in medical data that might remain undetected by clinicians (Cakmak *et al.* 2024; Cakmak and Pacal 2025). Using large datasets and sophisticated algorithms, we can enhance the accuracy of diagnosing, reduce human error, and enhance patient outcomes (Ozdemir and Pacal 2025; Pacal 2024a). Our study highlights the significant role ML plays in the diagnosis of anemia and other blood disorders, thus emphasizing the need for continued research and practical adaptation of these technologies. With early diagnosis and precise categorization, ML-based models would help the medical authorities offer better patient care, save on health care expenses, and proffer better public health outcomes (Ozdemir *et al.* 2025; Pacal and Attallah 2025b).

LITERATURE REVIEW

Sanap *et al.* (2011) conducted a study utilizing data mining techniques to predict and classify anemia, a prevalent blood disorder that can be categorized based on red blood cell morphology and etiology. The researchers constructed a dataset from complete blood count (CBC) test data obtained from various hospitals and evaluated the performance of two classification algorithms: the C4.5 decision tree algorithm and Support Vector Machine (SVM), implemented as J48 and Sequential Minimal Optimization (SMO) respectively, within the Weka software environment. Through a series of experiments, they generated a decision tree that facilitates optimal classification of anemia types and assesses anemia severity based on CBC reports. Their findings indicate that the C4.5 algorithm exhibits superior performance, achieving the highest accuracy in anemia classification.

Jaiswal *et al.* (2018) highlight the importance of machine learning in transforming healthcare data into meaningful insights for disease prediction and decision-making. Using CBC data from pathology centers, they evaluate Naïve Bayes, Random Forest, and Decision Tree algorithms for anemia classification. Their findings show that Naïve Bayes outperforms the other models in accuracy. Meena *et al.* (2019) examine childhood anemia, highlighting the impact of maternal health and diet during pregnancy. Using NFHS-4 survey data, they develop a decision support system with data mining techniques to predict anemia and guide prevention through dietary recommendations. Comparing decision tree and association rule mining, the study identifies the most effective method for predictive modeling in healthcare.

Yıldız *et al.* (2021) propose a decision support system for anemia detection using machine learning. Trained on 1,663 patient records from a Turkish hospital, the model classifies 12 anemia types based on hemogram data and medical history. Among the four algorithms tested, Bagged Decision Trees achieved the highest accuracy (85.6%), followed by Boosted Trees (83.0%) and Artificial Neural Networks (79.6%). The system aims to assist medical professionals and students in diagnosis. Asare *et al.* (2023) reviews machine learning applications for anemia detection, highlighting their affordability and non-invasive nature compared to traditional methods. They analyze current trends, algorithms, evaluation metrics, and dataset characteristics. The study finds that machine learning techniques offer a practical and efficient solution for anemia diagnosis, particularly in resource-limited settings. The results demonstrate that these methods enable timely and accessible detection, supporting their feasibility for clinical use.

Kilicarslan *et al.* (2021) explore deep learning for anemia prediction, emphasizing the need for tailored models due to dataset variability. They propose two hybrid models, GA-SAE and GA-CNN, which optimize Stacked Autoencoder (SAE) and Convolutional Neural Network (CNN) hyperparameters using a genetic algorithm (GA). The study classifies HGB-anemia, nutritional anemia (iron, B12, and folate deficiency), and non-anemic cases. Evaluated using accuracy, F-score, precision, and sensitivity, GA-CNN outperforms existing methods, achieving 98.50% accuracy.

Aslan and Özüpak (2024) investigate the integration of deep learning and image processing techniques for the classification of white blood cells (WBCs). In their study, they employed Convolutional Neural Network (CNN) models, specifically ResNet-50, VGG19, and a model they proposed, as feature extractors to enhance WBC classification accuracy. These CNN models were synergistically combined with Ridge feature selection and Maximal Information Coefficient (MIC) techniques to identify the most salient features and expedite the classification process. Consequently, they reported achieving a 98.27% success rate in the categorization of white blood cells, demonstrating a considerable improvement in classification accuracy with their proposed CNN model.

Alpsalaz *et al.* (2025) address the critical challenge of maize leaf disease diagnosis by proposing a lightweight and interpretable convolutional neural network (CNN) model for accurate and efficient classification. Utilizing the 'Corn or Maize Leaf Disease Dataset,' their model classifies four disease categories Healthy, Gray Leaf Spot, Common Rust, and Northern Leaf Blight achieving 94.97% accuracy and a micro-average AUC of 0.99. Emphasizing practical deployment, the model's minimal parameter count (1.22 million) supports real-time inference on mobile devices, facilitating field applications. The authors employed data augmentation and transfer learning for robust generalization, and Explainable Artificial Intelligence (XAI) methods (LIME and SHAP) to enhance transparency by identifying disease-relevant features, with SHAP achieving an IoU of 0.82. The proposed model outperformed benchmark architectures, including ResNet50, MobileNetV2, and EfficientNetB0, in both accuracy and computational efficiency. Furthermore, the model demonstrated adaptability with only a 2.82% performance drop under simulated extreme environmental conditions. These findings highlight the model's potential as a reliable, fast, and explainable solution for precision agriculture, particularly in resource-constrained settings.

MATERIALS AND METHODS

Dataset and Preprocessing

Anemi Dataset: This study utilizes a dataset consisting of 1281 rows and 15 features to classify anemia and other blood disorders. However, 49 duplicate records were removed, and the models were trained on the remaining 1232 rows. The target classes in the dataset include Healthy (HLT), Iron deficiency anemia (IDA), Leukemia (LEU), Leukemia with thrombocytopenia (LwT), Macrocytic anemia (MAA), Normocytic hypochromic anemia (NHA), Normocytic normochromic anemia (NNA), Other microcytic anemia (OMA), and Thrombocytopenia (THP) (Kaggle 2025).

The aim of this research is to employ machine learning techniques to classify the different types of anemia. Anemia is a significant global health issue, and its early diagnosis and accurate classification are essential for effective treatment and management. Proper classification of these disorders has the potential to improve treatment efficacy and healthcare management, thus contributing to better patient outcomes. The distribution of classes in the dataset used in the study is shown in Figure 1.

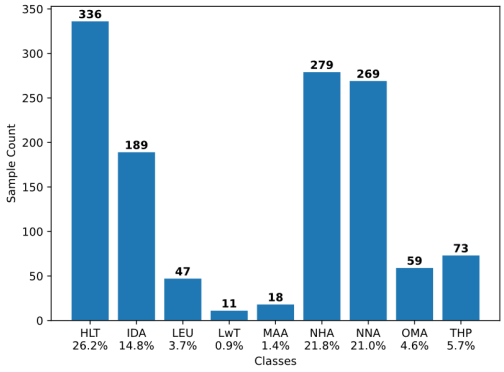

Figure 1 The distribution of classes in the dataset used in the study is shown

Characteristics and Classes of The Dataset: This study investigates key hematological features that play a vital role in the classification of anemia and related blood disorders. Each feature provides insights into specific aspects of blood cell composition and function. The characteristics and their corresponding attributes are summarized in Table 1.

Data Preprocessing Steps: The dataset underwent several preprocessing steps to enhance the quality and efficiency of the training process. Initially, missing values were handled by either removing the rows with null values or imputing them using statistical methods such as averaging or the median. Feature scaling was applied to ensure that all variables were within a comparable range, which is particularly important for models that rely on distance-based measurements. For categorical variables, encoding methods like one-hot or label encoding were used to convert them into numerical values. Since the target variable was already in a suitable format for classification, no logarithmic transformation was applied.

Additionally, duplicate records (49 instances) were identified and removed to avoid redundancy in the dataset. The dataset was then split into 80% for training and 20% for testing, as shown in Figure 2.

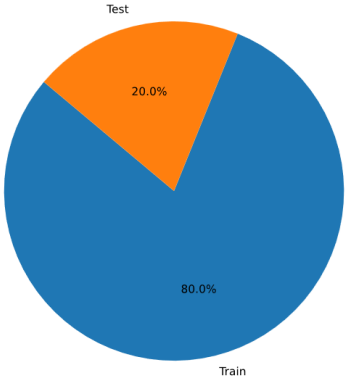

Figure 2 The dataset used in the study was divided into train 80% and test 20%

Algorithms Used

The machine learning algorithms employed in this study are detailed and explained in Table 2. These algorithms were carefully chosen for their proven effectiveness in classification tasks and their ability to handle complex, high-dimensional datasets. Each algorithm has unique characteristics that contribute to its performance in classifying anemia and other blood disorders. The selection process was based on the algorithms' strengths in terms of accuracy, efficiency, and ability to capture intricate patterns within the data. Below is a summary of each algorithm's approach and its relevance to the objectives of the study. Figure 3 shows some machine learning architectures.

The Decision Tree (DT) is a widely applied supervised learning algorithm for both classification and regression, constructing a tree-like model by recursively partitioning the dataset into smaller, more homogeneous subgroups based on feature values that maximize information gain or minimize impurity at each split (Muyama *et al.* 2024). Valued for their interpretability and efficiency with small to medium-sized datasets (Islam *et al.* 2024), DTs are prone to overfitting if allowed to grow excessively deep, learning noise and peculiarities from the training data which can hinder generalization. To mitigate this in this study, specific hyperparameter configurations were deliberately chosen: the max-depth of the tree was explicitly set to 6 to control complexity and prevent overfitting, while random-state was set to 42 to ensure the reproducibility of results. Although a more exhaustive hyperparameter search could explore other parameters like min-samples-split or criterion, constraining max-depth is a fundamental and effective strategy to balance the model's learning capacity with its ability to generalize to unseen data, a crucial aspect for reliable classification performance (Kasthuri *et al.* 2024).

Random Forest (RF) is a powerful ensemble learning algorithm that constructs a multitude of decision trees during training and outputs the class that is the mode of the classes (classification) or mean prediction (regression) of the individual trees. By training each tree on random subsets of both data samples (bagging) and features, RF aims to improve classification accuracy and robustness, effectively mitigating the overfitting tendency often seen in individual decision trees (Muyama *et al.* 2024).

This ensemble approach helps reduce both variance and bias, leading to more reliable and generalized predictions. RF is also known for its efficiency in handling high-dimensional data, its capability to manage missing values, and its scalability with large datasets. While RF excels at preventing overfitting and achieving high accuracy, its improved performance can come at the cost of increased computational resources and reduced interpretability compared to a single decision tree, due to the large number of trees involved.

In this study, to leverage these strengths while ensuring consistent results, the Random Forest classifier was configured with n-estimators set to 100, indicating that the forest was composed of 100 individual decision trees. The random-state was set to 42 to ensure the reproducibility of the model's training and subsequent predictions. While other hyperparameters such as max-depth for individual trees or min-samples-split could be further tuned, the choice of 100 estimators is a common and often effective starting point for balancing predictive power with computational load, aiming to harness the collective wisdom of the ensemble for robust classification.

Gradient Boosting (GB) is an ensemble learning technique that sequentially builds a strong predictive model from a collection of weak learners, typically decision trees. The core principle involves iteratively fitting new models to the residuals (errors) of the previous models, thereby progressively reducing bias and enhancing overall model accuracy. This additive training process allows GB to effectively model complex relationships in data for both regression

Table 1 Dataset features and descriptions

Features	Description
WBC	White Blood Cell count, indicating the number of white blood cells in the blood, used to assess immune function.
LYMp	Percentage of lymphocytes in the total white blood cell count, indicating immune response.
NEUTp	Percentage of neutrophils in the total white blood cell count, associated with bacterial infections.
LYMn	Absolute number of lymphocytes in the blood, providing a measure of immune function.
NEUTn	Absolute number of neutrophils in the blood, important in detecting bacterial infections.
RBC	Red Blood Cell count, reflecting the number of red blood cells that carry oxygen throughout the body.
HGB	Hemoglobin level in the blood, indicating the oxygen-carrying capacity of the blood.
HCT	Hematocrit, the proportion of blood volume occupied by red blood cells, used to diagnose anemia.
MCV	Mean Corpuscular Volume, representing the average size of red blood cells, important in anemia classification.
MCH	Mean Corpuscular Hemoglobin, indicating the average amount of hemoglobin per red blood cell.
MCHC	Mean Corpuscular Hemoglobin Concentration, measuring the average concentration of hemoglobin in red blood cells.
PLT	Platelet count, reflecting the number of platelets in the blood, crucial for blood clotting.
PDW	Platelet Distribution Width, measuring the variation in platelet size, which can indicate platelet disorders.
PCT	A procalcitonin test can help your health care provider diagnose if you have sepsis from a bacterial infection or if you have a high risk of developing sepsis.
Diagnosis	The target variable indicating the type of anemia or blood disorder diagnosis.

Table 2 Observed data for the DT algorithm

Class	Precision %	Recall %	F1-Score %	Support
HLT	98.0	98.0	98.0	64
IDA	100.0	100.0	100.0	44
LEU	91.0	100.0	95.0	10
LwT	80.0	80.0	80.0	5
MAA	100.0	100.0	100.0	4
NHA	100.0	98.0	99.0	49
NNA	98.0	100.0	99.0	52
OMA	100.0	86.0	92.0	7
THP	100.0	100.0	100.0	12
Macro avg	96.0	96.0	96.0	247
Weighted avg	96.0	98.0	98.0	247

and classification tasks across diverse data types and distributions. However, without careful tuning, GB can be susceptible to overfitting, particularly with a large number of iterations or excessive weight given to individual learners.

Regularization techniques, such as shrinkage (controlled by the learning rate) and subsampling (stochastic gradient boosting), are commonly employed to mitigate overfitting and improve model generalization (Mwangi *et al.* 2024). In this study, the Gradient Boosting Classifier was specifically configured with n-estimators (the number of boosting stages or trees) set to 100, a learning-rate of 0.1, and a max-depth of 6 for each individual tree. The random-state was set to 42 to ensure reproducibility. These hyperparameter settings were chosen to harness GB's predictive power: the n-estimators and learning-rate together control the complexity and learning speed of the ensemble, while max-depth limits the complexity of individual weak learners, collectively aiming for a robust model that accurately captures underlying data patterns without succumbing to overfitting.

Extreme Gradient Boosting (XGBoost), an acronym for Extreme Gradient Boosting, represents an advanced and optimized implementation of the gradient boosting framework, designed for superior computational efficiency, scalability, and predictive performance. It constructs an ensemble of decision trees sequentially, where each new tree aims to correct the errors made by the preceding ones (Kasthuri *et al.* 2024).

XGBoost distinguishes itself from traditional gradient boosting through several key enhancements, including built-in L1 (Lasso) and L2 (Ridge) regularization methods to combat overfitting and improve model generalization (Olatunji *et al.* 2024). Furthermore, it employs a more sophisticated optimization process utilizing second-order Taylor expansions (Hessians) in addition to first-order gradients, facilitating more precise model updates and potentially faster convergence.

Features such as parallel processing for tree construction and advanced tree pruning techniques contribute to its efficiency in terms of both time and computational resources, making it a highly popular choice in machine learning competitions and diverse real-

world applications for classification, regression, and ranking tasks, often achieving state-of-the-art results (Mwangi *et al.* 2024). In this study, the XGBoost classifier was configured with n-estimators (number of boosting rounds) set to 100, a learning-rate of 0.1, and a max-depth of 6 for individual trees. To ensure compatibility and suppress warnings, use-label-encoder was set to False, and logloss was specified as the eval-metric. The random-state was fixed at 42 for reproducibility. These specific hyperparameter settings were chosen to effectively leverage XGBoost's capabilities, balancing the model's complexity (via max-depth and n-estimators) with its learning pace (learning-rate) to achieve robust and accurate classification performance.

Categorical Boosting (CatBoost) is an advanced gradient boosting algorithm renowned for its robust handling of categorical data, often without requiring extensive preprocessing, which can be time-consuming with other methods. Based on decision trees, CatBoost builds an ensemble by sequentially adding trees, where each new tree corrects the errors made by its predecessors.

A key distinguishing feature of CatBoost is its sophisticated internal processing of categorical features, employing techniques like ordered target statistics that implicitly encode them without distorting their inherent structure, thereby simplifying feature engineering and enhancing modeling efficiency, especially with high-cardinality categorical variables. Furthermore, CatBoost incorporates ordered boosting and strategies for growing symmetric trees, which help mitigate overfitting and improve model generalization. The algorithm also offers built-in support for missing data and often demonstrates competitive speed and accuracy compared to traditional gradient boosting implementations.

Due to its high performance and often requiring minimal tuning, it has gained widespread adoption in machine learning competitions and real-world applications (Mwangi *et al.* 2024). In this study, the CatBoost classifier was specifically configured with iterations (number of trees) set to 100, learning-rate to 0.1, and depth (maximum depth of the trees) to 6. The verbose parameter was set to 0 to suppress training output. These hyperparameter choices aim to harness CatBoost's strengths in a controlled manner, with the learning rate influencing the contribution of each tree, the number of iterations determining the ensemble size, and the depth controlling individual tree complexity, all contributing to a balance between model expressiveness and its ability to generalize effectively from the training data.

RESULTS AND DISCUSSION

Decision Trees (DT)

The DT algorithm performs impressively well in classifying problems, boasting of overall accuracy that stands at a high 98%. The model, for the most part, established quite a high precision and recall among its classes, where perfect classification results, that is, 100%, in precision and recall, were achieved for class 1. The precision and recall of other classes well within high thresholds allowed macro-and weighted average F1 scores to be computed at 96% and 98%, respectively. These scores indicate that the predictive model's precision and recall are balanced across all classes. While slightly poorer performance was seen across smaller classes, the ability of the vast bandwidth of instances to be classified denotes effectiveness by the model on the dataset. The performance results of the DT algorithm discussed in this paragraph predestine high potential in regard to accurately classifying distinct types of anemia and blood disorders and being a very helpful instrument in diagnostic tasks. The observed data to the DT algorithm are shown in Table 2, while the confusion matrix is shown in Figure 4.

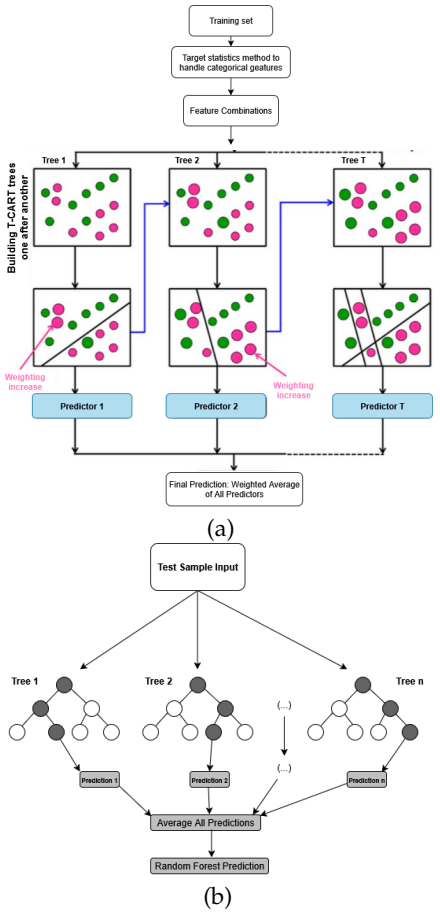

Figure 3 Models based on CatBoost and RF algorithms are provided in a and b, respectively (Pandey *et al.* 2023)

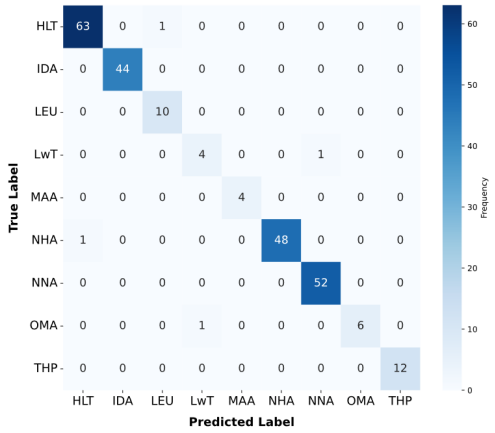

Figure 4 The Confusion Matrix obtained from the DT algorithm

Random Forest (RF)

The RF algorithm showed strong performance with an overall accuracy of 97%. Hence, this model is highly effective in classifying various types of anemia and blood disorders. In a class-wise breakdown, class 1 (Iron deficiency anemia) had both precision and recall and F1-score with a perfect score of 100%. Note that class 3 (Leukemia with thrombocytopenia) and class 4 (Macrocytic

anemia) had lower recall and F1 scores at 40% and 50% respectively. Yet the general performance of the model is solid, highlighted by a macro-average and a weighted average F1 score of 89% and 96% respectively. These results indicate the RF algorithm to be effective in providing accurate classification for the majority of the classes, leaving however an avenue for improvement on the management of certain lesser-represented categories. The observed data for RF algorithm is shown in Table 3 and the confusion matrix is shown in Figure 5.

Table 3 Observed data for the RF algorithm

Class	Precision %	Recall %	F1-Score %	Support
HLT	97.0	100.0	98.0	64
IDA	100.0	100.0	100.0	44
LEU	90.0	90.0	90.0	10
LwT	100.0	40.0	57.0	5
MAA	100.0	50.0	67.0	4
NHA	98.0	96.0	97.0	49
NNA	96.0	100.0	98.0	52
OMA	100.0	100.0	100.0	7
THP	86.0	100.0	92.0	12
Macro avg	96.0	86.0	89.0	247
Weighted avg	97.0	97.0	96.0	247

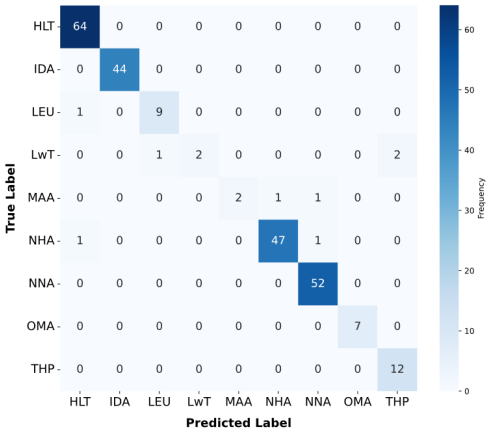

Figure 5 The Confusion Matrix obtained from the RF algorithm

Categorical Boosting (CatBoost)

The CatBoost algorithm showed excellent classification performance and achieved an overall accuracy of 98%, which means that the model is potentially very good at attacking various types of anemia and disorders of blood. Class 1, Iron deficiency anemia, had perfect precision, recall, and F1-score, indicating a very strong model for this class. Class 3, Leukemia with thrombocytopenia, had support for recall, where 80% of instances which belong to this class were, in fact, detected by the model. Class 4, Macrocytic anemia, had its complementary value for recall as 75%, because, although it was lower than the other classes, the model was able to classify a very good proportion of the instances for this class. Overall, the CatBoost model was efficient for all classes, which was revealed by high macro and weighted average F1-scores of 96% and 98%, respectively. These results confirm the effectiveness of the CatBoost algorithm in its classification task. The observed data for the CatBoost algorithm is displayed in Table 4, whilst Figure 6 illustrates the confusion matrix.

Table 4 Observed data for the CatBoost algorithm

Class	Precision %	Recall %	F1-Score %	Support
HLT	98.0	100.0	99.0	64
IDA	100.0	100.0	100.0	44
LEU	91.0	100.0	95.0	10
LwT	100.0	80.0	89.0	5
MAA	100.0	75.0	86.0	4
NHA	100.0	94.0	97.0	49
NNA	95.0	100.0	97.0	52
OMA	100.0	100.0	100.0	7
THP	100.0	100.0	92.0	12
Macro avg	98.0	86.0	96.0	247
Weighted avg	98.0	98.0	98.0	247

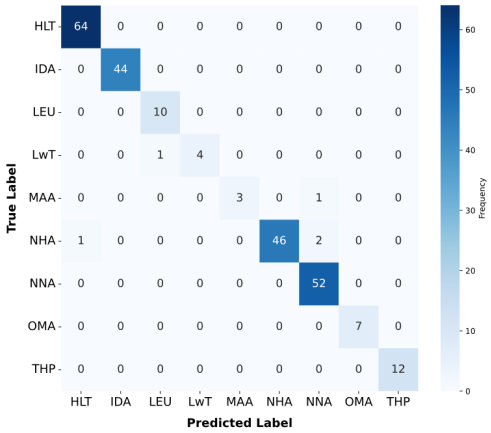

Figure 6 The Confusion Matrix obtained from the CatBoost algorithm

Gradient Boosting (GB)

This GB model incredibly has done well with an analysis of 99%, which demonstrated its superior performance. Some classes specifically two and three for leukemia and leukemia with thrombocytopenia, respectively were scored absolutely perfect for both precision, recall, and F1, so the model successfully scored these

classes. Class four, Macrocytic Anemia, also demonstrated perfect classification. Class seven, other microcytic anemia, would have a recall of 86% yet has still got some decent performance as shown with an F1 score of 92%. The macro average of F1 score is further enhanced by an overall score of 99%, while a weighted average F1 score of 99% underscores the model's classification quality. These results demonstrate the great advance provided by the GB algorithm in this task, with very consistent and reliable performance across all classes. The results of GB and some data for confusion matrices are shown in Table 5 and Figure 7, respectively.

Table 5 Observed data for the GB algorithm

Class	Precision %	Recall %	F1-Score %	Support
HLT	98.0	100.0	99.0	64
IDA	100.0	100.0	100.0	44
LEU	100.0	100.0	100.0	10
LwT	100.0	100.0	100.0	5
MAA	100.0	100.0	100.0	4
NHA	98.0	98.0	98.0	49
NNA	100.0	100.0	100.0	52
OMA	100.0	86.0	92.0	7
THP	100.0	100.0	100.0	12
Macro avg	100.0	98.0	99.0	247
Weighted avg	99.0	99.0	99.0	247

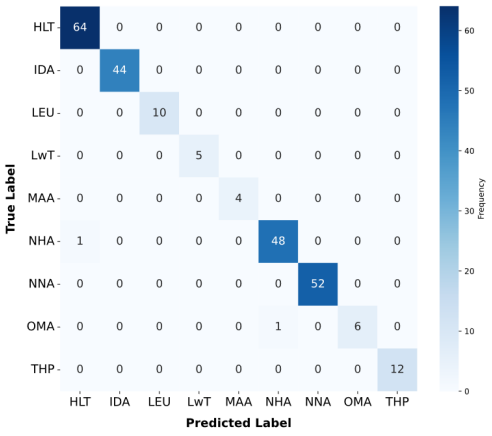

Figure 7 The Confusion Matrix obtained from the CatBoost algorithm

Extreme Gradient Boosting (XGBoost)

The XGBoost algorithm performed very well as well, getting an accuracy level of 98%. The model's precision and recall scores were outstanding for several classes, including class 1 (i.e., Iron deficiency anemia) and class 6 (i.e., Normocytic normochromic anemia), both of which showed perfect values of 100% precision, recall, and F1-scores. Class 2 demonstrated good scoring with precision metrics of 91% and perfect recall measures. However, class 3 recorded lower recalls: it was around 40%, which affected its F1-score, to about 57%, still. Nevertheless, the overall macro and weighted averages of 93% F1-value and 98% F1-value, respectively, indicate that the XGBoost model has performed well in the classification task. Therefore, it can be inferred that XGBoost tends to be an exceptionally capable algorithm for anemia classification, with lots of room for improvement for some classes. Observed data for the XGBoost algorithm is presented in Table 6, while the confusion matrix is presented in Figure 8.

Table 6 Observed data for the XGBoost algorithm

Class	Precision %	Recall %	F1-Score %	Support
HLT	98.0	100.0	99.0	64
IDA	100.0	100.0	100.0	44
LEU	91.0	100.0	95.0	10
LwT	100.0	40.0	57.0	5
MAA	100.0	100.0	100.0	4
NHA	98.0	98.0	98.0	49
NNA	100.0	100.0	100.0	52
OMA	100.0	86.0	92.0	7
THP	86.0	100.0	92.0	12
Macro avg	97.0	92.0	93.0	247
Weighted avg	98.0	98.0	98.0	247

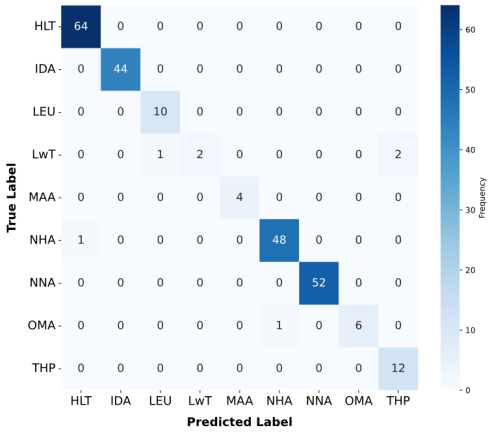

Figure 8 The Confusion Matrix obtained from the XGBoost algorithm

Feature Importance Analysis

The bar chart presented illustrates the feature importance scores determined by the GB model. In this case, the importance is derived from the magnitude of the absolute values of the model's coefficients, reflecting the degree to which each feature influences the

classification decision (Azimjonov and Kim 2024). "HGB" emerges as the most significant feature, followed by "MCH" and "MCHC," with higher coefficient magnitudes indicating their critical role in distinguishing between the classes. Other features like "MCV," "PLT," and "WBC" also contribute meaningfully to the model's predictions. Conversely, features lower in the chart, such as "PDW," "NEUTp," and "LYMn," hold relatively less importance and thus have a reduced impact on the decision boundary. Overall, the feature importance analysis emphasizes the central role of HGB, MCH, and MCHC-based attributes in the classification process, underscoring their relevance in hematological analysis and the diagnosis of anemia and related blood disorders. Figure 9 presents the feature importance plot for the GB algorithm (Got *et al.* 2024).

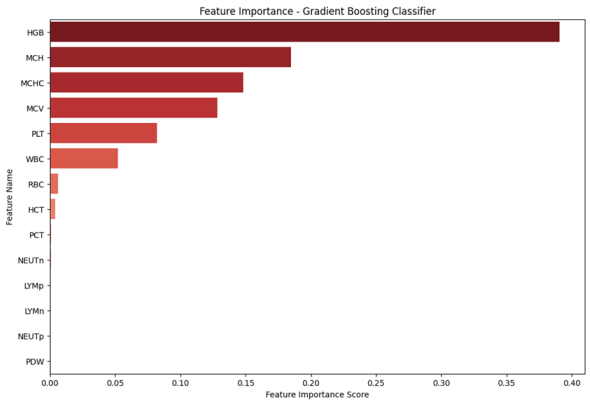

Figure 9 Illustrates the feature importance plot for the GB algorithm, highlighting the relative significance of each feature in the model's classification process

DISCUSSION

This section introduces an autonomous diagnostic approach based on machine learning for the diagnosis of anemia, a prevalent and clinically significant blood disorder. In this study, several commonly used machine learning algorithms, selected from the existing literature for their proven efficacy in similar classification tasks, were trained and tested on anemia-related data. The primary aim was to identify the most accurate model for distinguishing anemic cases. The experimental results, specifically the accuracy achieved by each algorithm, are systematically presented in Table 7 below. This table offers a direct comparison of the predictive capabilities of the tested models when applied to the Anemi dataset.

Table 7 The experimental results of the ML algorithms tested on the Anemi dataset

Rank	Models	Accuracy %
1	Gradient Boosting	99.19
2	Decision Tree	98.38
3	CatBoost	97.98
4	XGBoost	97.98
5	Random Forest	96.76

As evident from Table 8, the GB model stands out as the top-performing algorithm, achieving an impressive accuracy of 99.19%. Such exceptional performance underscores the model's capacity to iteratively correct its mistakes and produce highly refined predictions, making it particularly well-suited for complex classification tasks like anemia diagnosis and suggesting its strong potential as a core component in an automated anemia screening tool. Other models also demonstrated commendable performance. The DT algorithm achieved a high accuracy of 98.38%, often effective in capturing interactions among input features. CatBoost, with an accuracy of 97.98%, also performed superbly, its strength lying in its optimized handling of categorical features combined with gradient boosting techniques. XGBoost achieved an identical accuracy of 97.98%, while RF followed closely with 96.76% (Kasthuri et al., 2024). While these models also exhibited strong predictive power, they did not quite match the benchmark set by GB. Nevertheless, both XGBoost and RF are robust ensemble methods, known for their tree-based nature and capabilities in managing feature interactions, with RF, in particular, mitigating overfitting by averaging predictions from multiple decision trees.

It is crucial to acknowledge that model performance is significantly dependent on factors such as feature selection, data preprocessing, and meticulous hyperparameter tuning; further fine-tuning could potentially lead to even greater performance. Beyond predictive accuracy, computational efficiency is an important consideration for real-world clinical applications. While GB yielded the highest accuracy, it can be computationally more intensive. In contrast, algorithms like RF and XGBoost might offer better scalability. Future work could explore advanced feature engineering, hybrid models, and leveraging deep learning architectures. Crucially, incorporating explainability methods such as SHAP values or LIME will be vital for providing transparency into model decisions, thereby fostering trust and facilitating the adoption of AI-assisted anemia diagnostic systems in clinical practice (Awe *et al.* 2024).

CONCLUSION

This research compellingly demonstrates the transformative potential of machine learning algorithms in enhancing the early detection and precise classification of anemia and other hematological disorders, conditions often overlooked until they manifest severe consequences. Through the application of classical machine learning models, including DT, RF, CatBoost, GB, and XGBoost, on key hematological parameters such as red RBC, WBC, hemoglobin (HGB), and platelet count (PLT), this study identified Gradient Boosting as a particularly robust model, achieving an impressive accuracy of 99.19%. This high level of accuracy underscores the model's capacity to capture intricate, complex patterns within patient datasets, thereby enabling highly precise predictions and showcasing significant promises for medical diagnostics.

The findings emphasize how AI-powered diagnostic approaches can significantly augment clinical decision-making processes by facilitating faster, more reliable diagnoses and potentially reducing diagnostic errors, which is especially critical for conditions like anemia where timely intervention can substantially improve patient outcomes and mitigate complications. The widespread adoption of such autonomous diagnostic tools could also alleviate the burden on healthcare systems by expediting treatment planning.

Looking ahead, the continued refinement of these algorithms and the integration of more advanced techniques, such as deep learning or hybrid models, are anticipated to further elevate diag-

nostic accuracy and enhance the scalability of these solutions in clinical workflows. A crucial aspect of future development will be the implementation of explainable AI (XAI) methodologies, like SHAP or LIME. These techniques are vital for fostering greater trust and acceptance among healthcare professionals by providing transparency into the decision-making processes of the models, thereby supporting their integration into routine clinical practice. Ultimately, the progression of machine learning in the diagnosis and management of anemia and other blood disorders paves the way for more personalized, data-driven medical solutions, holding immense promise for improving patient care, optimizing healthcare delivery, and offering deeper insights into complex hematological conditions, moving us closer to the paradigm of precision medicine.

Ethical standard

The authors have no relevant financial or non-financial interests to disclose.

Availability of data and material

The data that support the findings of this study are available from the corresponding author upon reasonable request.

Conflicts of interest

The authors declare that there is no conflict of interest regarding the publication of this paper.

LITERATURE CITED

Alpsalaz, F., Y. Özüpak, E. Aslan, and H. Uzel, 2025 Classification of maize leaf diseases with deep learning: Performance evaluation of the proposed model and use of explicable artificial intelligence. Chemometrics and Intelligent Laboratory Systems p. 105412.

Aruk, I., I. Pacal, and A. N. Toprak, 2025 A novel hybrid convnext-based approach for enhanced skin lesion classification. Expert Systems with Applications p. 127721.

Asare, J. W., P. Appiahene, and E. T. Donkoh, 2023 Detection of anaemia using medical images: A comparative study of machine learning algorithms–a systematic literature review. Informatics in Medicine Unlocked **40**: 101283.

Aslan, E. and Y. Özüpak, 2024 Classification of blood cells with convolutional neural network model. Bitlis Eren Üniversitesi Fen Bilimleri Dergisi **13**: 314–326.

Awe, O. O., J. M. Adepoju, E. Boniface, and O. D. Awe, 2024 Comparative analysis of random forest and neural networks for anemia prediction in female adolescents: A lime-based explainability approach. In *Practical Statistical Learning and Data Science Methods: Case Studies from LISA 2020 Global Network, USA*, pp. 555–573, Springer.

Azimjonov, J. and T. Kim, 2024 Designing accurate lightweight intrusion detection systems for iot networks using fine-tuned linear svm and feature selectors. Computers & Security **137**: 103598.

Cakmak, Y. and I. Pacal, 2025 Enhancing breast cancer diagnosis: A comparative evaluation of machine learning algorithms using the wisconsin dataset. Journal of Operations Intelligence **3**: 175–196.

Cakmak, Y., S. Safak, M. A. Bayram, and I. Pacal, 2024 Comprehensive evaluation of machine learning and ann models for breast cancer detection. Computer and Decision Making: An International Journal **1**: 84–102.

Fentie, K., T. Wakayo, and G. Gizaw, 2020 Prevalence of anemia and associated factors among secondary school adolescent girls in jimma town, oromia regional state, southwest ethiopia. Anemia **2020**: 5043646.

Got, A., D. Zouache, A. Moussaoui, L. Abualigah, and A. Alsayat, 2024 Improved manta ray foraging optimizer-based svm for feature selection problems: a medical case study. Journal of Bionic Engineering **21**: 409–425.

Ince, S., I. Kunduracioglu, A. Algarni, B. Bayram, and I. Pacal, 2025 Deep learning for cerebral vascular occlusion segmentation: a novel convnextv2 and grn-integrated u-net framework for diffusion-weighted imaging. Neuroscience **574**: 42–53.

İnce, S., I. Kunduracioglu, B. Bayram, and I. Pacal, 2025 U-net-based models for precise brain stroke segmentation. Chaos Theory and Applications **7**: 50–60.

Islam, R., S. Tanweer, M. T. Nafis, I. Hussain, and O. Ahmad, 2024 Intelligent diagnosis of sickle cell anemia in chronic diseases through a machine learning predictive system. In *International Conference on ICT for Digital, Smart, and Sustainable Development*, pp. 109–124, Springer.

Jaiswal, M., A. Srivastava, and T. J. Siddiqui, 2018 Machine learning algorithms for anemia disease prediction. In *Recent trends in communication, computing, and electronics: Select proceedings of IC3E 2018*, pp. 463–469, Springer.

Kaggle, 2025 Anemia types classification.

Karra, M. L., E. A. Rahiman, M. Narahari, A. V. Bhongir, G. Rathod, *et al.*, 2025 Unveiling the burden of sickle cell anemia: A pilot study validating dried blood spots for newborn screening. Indian Journal of Pediatrics **92**: 405–408.

Kasthuri, E., S. Subbulakshmi, and R. Sreedharan, 2024 Insightful clinical assistance for anemia prediction with data analysis and explainable ai. Procedia computer science **233**: 45–55.

Kilicarslan, S., M. Celik, and Ş. Sahin, 2021 Hybrid models based on genetic algorithm and deep learning algorithms for nutritional anemia disease classification. Biomedical Signal Processing and Control **63**: 102231.

Kitaw, B., C. Asefa, and F. Legese, 2024 Leveraging machine learning models for anemia severity detection among pregnant women following anc: Ethiopian context. BMC Public Health **24**: 3500.

Krieg, S., S. Loosen, A. Krieg, T. Luedde, C. Roderburg, *et al.*, 2024 Association between iron deficiency anemia and subsequent stomach and colorectal cancer diagnosis in germany. Journal of Cancer Research and Clinical Oncology **150**: 53.

Li, C., X. Shi, S. Chen, X. Peng, and S. Zong, 2025 Novel mechanistic insights into the comorbidity of anemia and rheumatoid arthritis: Identification of therapeutic targets. Molecular Immunology **180**: 74–85.

Link, H., M. Kerkmann, L. Holtmann, and M. Detzner, 2024 Anemia diagnosis and therapy in malignant diseases: implementation of guidelines—a representative study. Supportive Care in Cancer **32**: 113.

Malak, M. Z., A. Shehadeh, A. Ayed, and E. Alshawish, 2025 Predictors of anemia among infants at the age of one year attending health centers in the west bank/palestine: a retrospective study. BMC Public Health **25**: 179.

Meena, K., D. K. Tayal, V. Gupta, and A. Fatima, 2019 Using classification techniques for statistical analysis of anemia. Artificial intelligence in medicine **94**: 138–152.

Muyama, L., A. Neuraz, and A. Coulet, 2024 Deep reinforcement learning for personalized diagnostic decision pathways using electronic health records: A comparative study on anemia and

systemic lupus erythematosus. Artificial Intelligence in Medicine **157**: 102994.
Mwangi, P., S. Kotva, and O. O. Awe, 2024 Explainable ai models for improved disease prediction. In *Practical Statistical Learning and Data Science Methods: Case Studies from LISA 2020 Global Network, USA*, pp. 73–109, Springer.
Olatunji, S. O., M. A. A. Khan, F. Alanazi, R. Yaanallah, S. Alghamdi, *et al.*, 2024 Machine learning-based models for the preemptive diagnosis of sickle cell anemia using clinical data. In *Finance and Law in the Metaverse World: Regulation and Financial Innovation in the Virtual World*, pp. 101–112, Springer.
Ozdemir, B., E. Aslan, and I. Pacal, 2025 Attention enhanced inceptionnext based hybrid deep learning model for lung cancer detection. IEEE Access .
Ozdemir, B. and I. Pacal, 2025 A robust deep learning framework for multiclass skin cancer classification. Scientific Reports **15**: 4938.
Pacal, I., 2024a Maxcervixt: A novel lightweight vision transformer-based approach for precise cervical cancer detection. Knowledge-Based Systems **289**: 111482.
Pacal, I., 2024b A novel swin transformer approach utilizing residual multi-layer perceptron for diagnosing brain tumors in mri images. International Journal of Machine Learning and Cybernetics **15**: 3579–3597.
Pacal, I. and O. Attallah, 2025a Hybrid deep learning model for automated colorectal cancer detection using local and global feature extraction. Knowledge-Based Systems p. 113625.
Pacal, I. and O. Attallah, 2025b Inceptionnext-transformer: A novel multi-scale deep feature learning architecture for multimodal breast cancer diagnosis. Biomedical Signal Processing and Control **110**: 108116.
Pandey, M., M. Karbasi, M. Jamei, A. Malik, and J. H. Pu, 2023 A comprehensive experimental and computational investigation on estimation of scour depth at bridge abutment: Emerging ensemble intelligent systems. Water Resources Management **37**: 3745–3767.
Ramzan, M., J. Sheng, M. U. Saeed, B. Wang, and F. Z. Duraihem, 2024 Revolutionizing anemia detection: integrative machine learning models and advanced attention mechanisms. Visual Computing for Industry, Biomedicine, and Art **7**: 18.
Sanap, S. A., M. Nagori, and V. Kshirsagar, 2011 Classification of anemia using data mining techniques. In *International conference on swarm, evolutionary, and memetic computing*, pp. 113–121, Springer.
Subba, S. S. and S. Araveti, 2025 Knowledge, attitudes, and practices related to iron deficiency anemia and probiotics among adolescent girls in anantapur, india: A qidap-guided cross-sectional study. Food and Humanity **4**: 100551.
Yıldız, T. K., N. Yurtay, and B. Öneç, 2021 Classifying anemia types using artificial learning methods. Engineering Science and Technology, an International Journal **24**: 50–70.
Yoshida, N., 2024 Recent advances in the diagnosis and treatment of pediatric acquired aplastic anemia. International journal of hematology **119**: 240–247.

How to cite this article: Cakmak, Y., and Pacal, I. AI-Driven Classification of Anemia and Blood Disorders Using Machine Learning Models. *Computers and Electronics in Medicine*, 2(2), 43-52, 2025.

ADBA
Computers and Electronics in Medicine
Cutting-Edge Scientific Solutions

e-ISSN: 3023-8609
RESEARCH ARTICLE
Vol.2 / No.2 / 2025 / pp.53-59
https://doi.org/10.69882/adba.cem.2025074

A Chaos-Based Encryption Scheme for Secure Medical X-ray Images

Yasin Kaya *,[1] **and Zeynep Gürkas Aydin** *,[2]
[1]Istanbul University-Cerrahpaşa, Department of Computer Engineering, Istanbul, Türkiye.

ABSTRACT Data privacy in healthcare system is getting more importance day by day. In this study we introduce a novel chaos-based encryption scheme for medical X-ray images. We used a double Lorenz map as chaotic system to produce random key streams in confusion phase and in diffusion phase. We also used hash value of the original file to determine initial parameters of second chaotic map. So, our scheme is highly resistant to differential attacks. In confusion phase, we employed row-based and column-based shift operation to confuse original data. In diffusion phase we used XoR operation to encrypt data. Since Lorenz map has 3 dimensions, we used each one for different purposes like X dimension is for row-based shift operation, Y dimension is for column-based shift operation, Z dimension is for data distribution, XoR operation etc. On average, our scheme generates a NPCR value exceeding 99.66% and an UACI value of approximately 33.39% when there is a one-pixel alteration in the plaintext. Additionally, it yields an average information entropy value greater than 7.9976. Since our method utilizes a double Lorenz map, it is resilient against brute force attacks. The results from our tests and analyses indicate that our schema is pretty fast, dependable, resilient, practical, and effective. It serves as a solid encryption scheme option for medical images.

KEYWORDS
Nonlinear dynamics
Chaos
Medical image encryption
Hash-Code
Security

INTRODUCTION

Medical image encryption has been a hot topic for several decades in terms of patient data privacy. Numerous encryption methods have been developed based on different ideas and systems to protect data from prying eyes or unauthorized access. One of the most popular systems is chaotic systems. Because of their anatomical characteristics, such as pseudo-randomness, ergodicity, high sensitivity to initial conditions and parameters, and aperiodicity, chaotic systems have become more popular in cryptography in recent years. Researchers have long benefited from chaotic systems in their studies since these characteristics are necessary for a strong encryption scheme (Malik *et al.* 2020; Mohammed *et al.* 2023; Abdelli *et al.* 2024).

In order to achieve much more successive and robust outcomes, researchers prefer using chaotic systems with other mathematical models like DNA (deoxyribonucleic acid) (Chai *et al.* 2017, 2019; Liu and Liu 2020; Wang *et al.* 2019; Zhou *et al.* 2022), Fourier Transform (Farah *et al.* 2020), Generative Adversarial Networks (Fang *et al.* 2021), Hilbert Curves and H-Fractals (Zhang *et al.* 2019), Knuth–Durstenfeld (Wang *et al.* 2020), Transcendental Numbers (Silva Garcia *et al.* 2019), Particle Swarm Optimization (Alibrahim and Ludwig 2021), Latin Square (Machkour *et al.* 2015), Rotor Machine (Rehman *et al.* 2020), and Discrete Wavelet Transform (DWT) (Oteko Tresor and Sumbwanyambe 2019).

In this study, we propose a chaos-based image encryption scheme to protect medical X-ray images. We used a dual Lorenz map, where the XOR operation is applied using the outcome of the second map and the number of shift steps for both rows and columns is determined using the first map. The secret key is the only source of input parameters for the first Lorenz map, whereas the hash value of the plaintext and the secret key are combined to provide the input parameters for the second Lorenz map. Our technique is highly resistant to differential attacks by using the plaintext hash value to set the input parameter for the second Lorenz map. When a single pixel in the plaintext changes, it typically generates a value of over 99.66% NPCR (number of pixels change rate) and over 33.39% UACI (unified average changing intensity). Additionally, it generates an average information entropy value of more than 7.9976.

When we look at the literature, we see that researchers have been using chaotic systems extensively in medical image encryption for several decades. Demirkol *et al.* (2024) proposed a novel locally active memristor-based chaotic circuit model and presented a real-time hybrid image encryption application developed on a PYNQ-Z1 (Python Productivity for Zynq) low-cost FPGA board using Jupiter programming environment. The proposed hybrid algorithm combines memristor-based chaos with a DNA encryption algorithm exploiting diffusion-confusion techniques.

Manuscript received: 26 May 2025,
Revised: 20 July 2025,
Accepted: 20 July 2025.

[1]ysnky@yahoo.com (**Corresponding author**)
[2]zeynepg@iuc.edu.tr

Kanwal *et al.* (2024) offered an IoT-Blockchain system based on chaos smart healthcare image encryption scheme using Tinkerbell mapping to ensure medical data integrity and authenticity. The suggested approach was examined to assess performance parameters such as key space analysis, key sensitivity analysis, Information Entropy (IE), histogram, correlation of adjacent pixels, Number of Pixel Change Rate (NPCR), Unified Average Changing Intensity (UACI), Peak Signal to Noise Ratio (PSNR), Mean Square Error (MSE), and Structural Similarity Index (SSIM). John and Kumar (2023) proposed a hybrid chaotic model, 2D Lorentz Chaotic model coupled with the Logistic chaotic model for the encryption/decryption of medical DICOM CT images. Prior to encryption, preprocessing was done by the median filter. The hybrid chaotic model scrambles the rows and columns of the image and bitwise XOR operation is carried out to generate the encrypted image. Ismail *et al.* (2018) proposed a medical image encryption algorithm based on pseudo-random sequence generation using the proposed generalized DH map offering secure communication transfer of medical MRI and X-ray images. Security analyses are carried out to consolidate system efficiency including key sensitivity and key-space analyses, histogram analysis, correlation coefficients, MAE, NPCR and UACI calculations.

Several other notable works have contributed to this field. Vijayakumar and Ahilan (2024) offered a new medical image encryption technology based on chaotic map substitution boxes (S-box) and cellular automata (CA). Qobbi *et al.* (2023) proposed a new method for medical image encrypting of arbitrary sizes and formats based on chaos with an S-box construction. Rehman *et a* (2023) presented a color medical image encryption scheme that integrates multiple encryption techniques, including alternate quantum random walks and controlled Rubik's Cube transformation Roy *et al.* (2025) offered an innovative framework that integrate healthcare engineering, chaotic encryption, and artificial intelligence (AI) to address the privacy issue of medical data. Dua and Bhogal (2024) proposed a medical image cryptosystem using one-dimensional novel Sine-Tangent Chaotic (STC) map and shared key. Masood *et al.* (2021) proposed a lightweight cryptosystem based on Henon chaotic map, Brownian motion, and Chen' chaotic system. Clemente-Lopez *et al.* (2024) proposed a chaos based lightweight encryption scheme for IoT healthcare system with a primary application in the encryption of wearable devices Kaya *et al.* (2025) proposed a novel lightweight encryption scheme for platforms with limited resources utilizing chaotic systems with a double logistic map, hash code of original file and cycle rotation.

The remainder of this paper is organized as follows. Section II presents the proposed encryption algorithm with chaotic map and the detailed methodology. Section III presents all experimental results and security analysis comparisons with other schemes. The conclusion is presented in the last section.

PROPOSED ALGORITHM

Numerous chaotic maps, ranging from basic to intricate architectures, exist, including the Henon, Lorenz, Tent, Arnold Cat, and Logistic maps. In our study we used 3-D Lorenz map in confusion and diffusion phase as pseudo random number generator. Each dimension of the map is used for a different process like X dimension is used for row-based shift operation while Y dimension is used for column-based shift operation and Z dimension is used for XoR operation. Two distinct Lorenz maps with various starting parameters were employed. Only the secret key is utilized to determine the first Lorenz map's initial parameter, and rows and columns of the plaintext are shuffled by using this key stream data for shift operations. We combined the hash value of the plaintext with the secret key to generate the initial parameters of the second Lorenz map and key stream data is utilized for XoR operation because our scheme needs to be sensitive to plaintext changes in order to withstand differential attacks.

Lorenz map

The Lorenz map is one of the most popular and widely used 3-D chaotic map, which is formulated as shown below in Eqs. (1)-(3):

$$\frac{dx}{dt} = \sigma(y - x) \tag{1}$$

$$\frac{dy}{dt} = x(\rho - z) - y \tag{2}$$

$$\frac{dz}{dt} = xy - \beta z \tag{3}$$

Here, σ, ρ and β are constant parameters and generally used the values $\sigma = 10$, $\rho = 28$, and $\beta = \frac{8}{3}$. When these (and similar) values are present, the system behaves chaotically. Lorenz map attractor can be viewed in Figure 1.

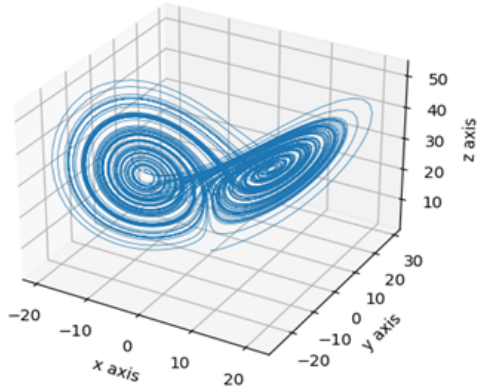

Figure 1 : Lorenz map attractor

Hash function

The fundamental purpose of hash functions is to obtain a tiny input data signature. The hash value is the result of the hash function. A successful hash function must be sensitive to even the smallest changes in the input data, meaning that even small changes should result in noticeably different hash values. Many hash functions, including SHA-1, SHA-2, SHA-3, MD5, BLAKE, xxHash and others, are now in use. Since xxHash is known as the speediest hash function we choose it in our study.

Shuffling algorithm

In the permutation phase, we employed row-based and column-based shift operations to shuffle the plaintext. Each row and each column are shifted n times which are generated by the first Lorenz map X dimension and Y dimension respectively. In decryption process we applied column-based and row-based shift operations in reverse direction to obtain unshuffled data from shuffled data.

Encryption Process

Initially, we calculate the plaintext's hash value, pick just the first two bytes of this value, and refer to it as H_2. To create pseudo random values that will be utilized in the XOR operation a step later, we utilize H_2 with a secret key as input parameters of the second Lorenz map. Next, we use key stream for row-based and column-based shift operations in the permutation phase, and we start the first Lorenz map with just a secret key as an input parameter. Then, we use a second Lorenz map key stream to perform the XOR operation on this shuffled data.

Using the H_2 value we create 1-byte validation value and used it with H_2 value as 3-byte HV_3 value. The repeating HV_3 values are then added to a new row that is added at the bottom of the matrix. Assuming, for instance, that the matrix column size is 210, the newly inserted row will have 70 times HV_3 values sequentially $(210/3 = 70)$. To safeguard the HV_3 values, we then execute the XOR operation to this row using the first Lorenz map key stream. In the final phase, we use the indexes produced by the first Lorenz map to distribute this new row data into the XORed matrix by swap operation. Consequently, the final ciphertext was acquired. Figure 2 shows all encryption processes.

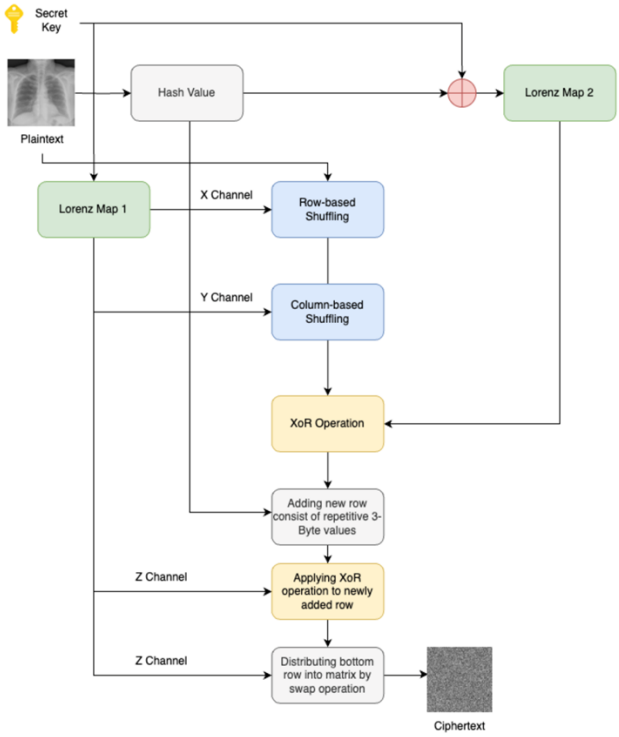

Figure 2 :Encryption process of proposed scheme

Decryption Process

To decrypt the ciphertext, the encryption operations are applied in reverse order. First, using the indices generated by the first Lorenz map, a swap operation is performed to retrieve the XORed HV_3 values and place them at the bottom row of the matrix. To recover the original HV_3 sequence, an XOR operation is then applied to this row using the corresponding key stream. Since the data may be affected by external factors such as noise or cropping attacks, validating the integrity of the HV_3 value is essential.

A validation procedure is carried out to ensure the correctness of HV_3, and only the most frequently occurring valid HV_3 value is accepted. Once the valid HV_3 value is identified, the last row is removed from the matrix, and its final byte is discarded to retrieve the H_2 value. This extracted H_2, in combination with the secret key, is then used to initialize the second Lorenz map. The resulting key stream is used to perform an XOR operation on the encrypted matrix to reverse the diffusion process.

Finally, inverse shift operations are performed on the resulting matrix — first column-based and then row-based — using the key streams generated by the first Lorenz map. As a result, the original plaintext is successfully recovered. All decryption steps are illustrated in Figure 3.

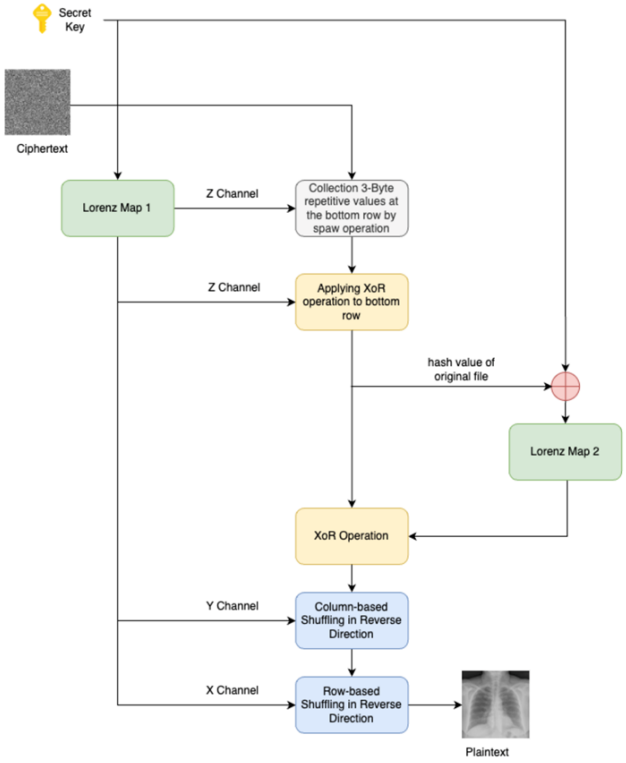

Figure 3 :Decryption process of proposed scheme

Figure 4 presents the original X-ray image (256×256 grayscale), the encrypted image obtained using the proposed scheme, and the corresponding decrypted image, respectively.

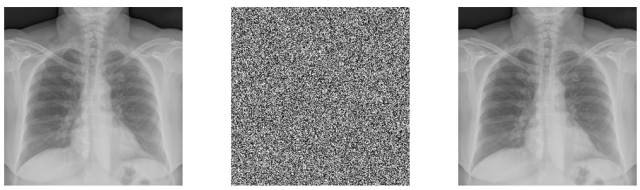

Figure 4 Scheme outputs: (a) plaintext, (b) ciphertext, (c) original plaintext.

EXPERIMENTAL RESULTS

In this section, we have conducted numerous simulated analyses and experimental tests to assess the safety, effectiveness, and robustness of our method. In our tests, we used some of medical X-ray images, like "Chest", "Foot", "Hand" and "Joint" in 256x256

grayscale format. These data are publicly available and taken from Kaggle. We tested our algorithm on a Mac OS X (Sequoia) with Apple M1 pro processor and 16 GB of RAM after developing it with Python 3.9.2.

Information Entropy Analysis

A cryptosystem's entropy value indicates how resilient the algorithm is against entropy attacks. Entropy essentially measures how randomly the pixels in an image are distributed. The calculation of information entropy is given below equation:

$$H(X) = \sum_{i=1}^{n} P_r(x_i) \log_2 \left(\frac{1}{P_r(x_i)} \right)$$

where X denotes the input image, x_i denotes a pixel value, and $P_r(x_i)$ denotes the probability of x_i. Truly random entropy value for a 2^n symbol data is n. Since there are 256 different colors and $2^8 = 256$, the truly random entropy value is 8 for a grayscale image. The algorithm appears more secure when the entropy value converges to a truly random entropy value, which is 8 in this case. Our test results are shown in Table 1 and represent satisfactory results by converging to a truly random entropy value of 8.

Table 1 Information Entropy Values of Plain and Encrypted Medical Images

Image	Size	Plain Image Entropy	Cipher Image Entropy
Chest	256×256	7.037043	7.996937
Foot	256×256	6.924769	7.997189
Hand	256×256	7.000145	7.997503
Joint	256×256	7.206429	7.997263

Histogram Analysis

The distribution of pixel frequencies in an image can be seen by histogram analysis. Histogram analysis is crucial for an encrypted image, and a balanced pixel value distribution is intended to withstand statistical attacks. The histogram leaks information about the original image and provides attackers with hints about it if it lacks a balanced distribution. The histogram analysis of both plain and encrypted images is shown in Figure 5. In contrast to the original images' histograms, the encrypted images' histograms show a distribution that is comparatively uniform.

Correlation Analysis

In terms of diagonal, vertical, and horizontal neighborhoods, there is a strong association between neighboring pixels in an image. It provides attackers with a wealth of information about the original image. Therefore, these correlations must be destroyed by a secure encryption scheme. This is measured using the correlation coefficient value between Eqs.(5)-(8) that is computed as follows:

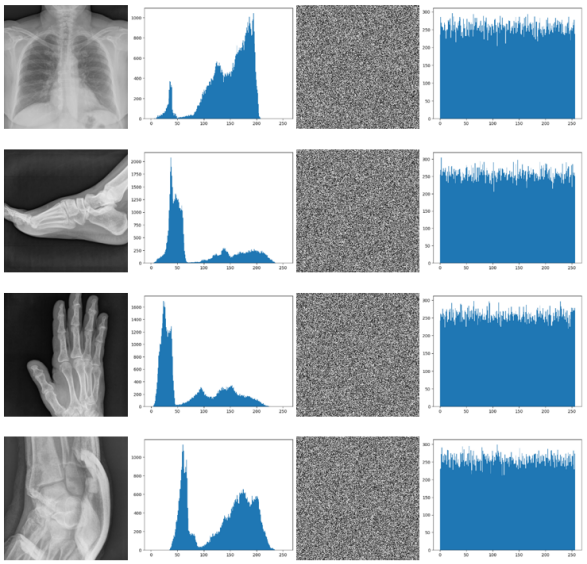

Figure 5 : Histogram analysis; the first column is original images, the second column is histograms of the original images, the third column is encrypted images, the fourth column is histograms of the encrypted images

$$r_{xy} = \frac{\mathrm{cov}(x,y)}{\sqrt{D(x)}\sqrt{D(y)}} \tag{5}$$

$$\mathrm{cov}(x,y) = \frac{1}{N}\sum_{i=1}^{N}(x_i - E(x))(y_i - E(y)) \tag{6}$$

$$D(x) = \frac{1}{N}\sum_{i=1}^{N}(x_i - E(x))^2 \tag{7}$$

$$E(x) = \frac{1}{N}\sum_{i=1}^{N} x_i \tag{8}$$

where two neighboring pixels in the image have grayscale values denoted by x and y. 10,000 neighboring pixels were chosen at random for our test in order to compute the horizontal, vertical, and diagonal correlations for each plain and encrypted image. Figure 6 displays the outcomes of our tests, and Table 2 lists the correlation coefficient values. The correlation analysis results produced by our scheme are satisfactory.

Table 2 Correlation Coefficient Values of Plain and Encrypted Images

Image	Plain H	Plain V	Plain D	Enc. H	Enc. V	Enc. D
Chest	0.9957	0.9937	0.9912	0.0139	0.0052	-0.0124
Foot	0.9970	0.9916	0.9895	-0.0134	0.0002	0.0016
Hand	0.9874	0.9965	0.9856	0.0145	-0.0181	-0.0052
Joint	0.9909	0.9969	0.9897	-0.0029	0.0108	-0.0002

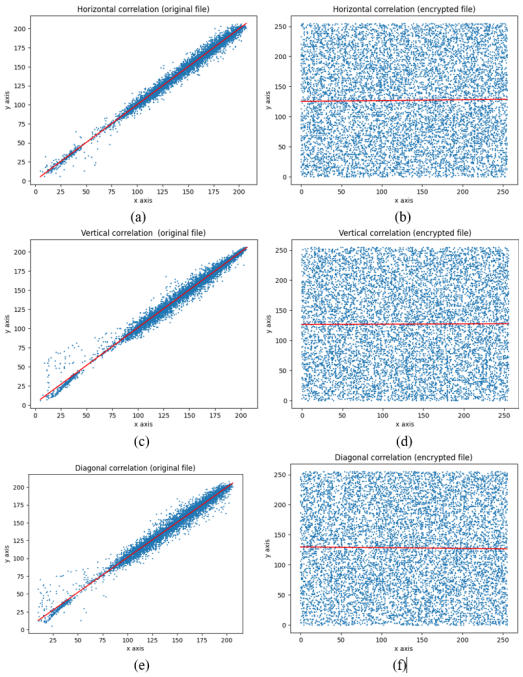

Figure 6 Correlation analysis of Chest image: (a) plain image horizontal correlation, (b) encrypted image horizontal correlation, (c) plain image vertical correlation, (d) encrypted image vertical correlation, (e) plain image diagonal correlation, (f) encrypted image diagonal correlation.

Differential attack analysis

Attackers try everything to find out the original data. In one method, the input plain image is slightly altered, and then both the original and altered images are encrypted. Next, a significant association between the plain and encrypted images is found. To assess the effect of altering a single pixel in the plaintext on the encrypted image, two metrics, Number of Pixels Change Rate (NPCR) and Unified Average Changing Intensity (UACI) have been created. NPCR is defined as the proportion of different pixel intensities between the plain and cipher images. Conversely, UACI is the average strength of the differences between the plain and cipher images. NPCR is formulated as in Eq. (9),

$$\text{NPCR} = \frac{\sum_{i,j} S(x,y)}{N \times M} \times 100\% \tag{9}$$

where M and N are the dimensions of the image and $S(x,y)$ is expressed as in Eq. (10):

$$S(x,y) = \begin{cases} 1, & \text{if } C_1(x,y) \neq C_2(x,y) \\ 0, & \text{if } C_1(x,y) = C_2(x,y) \end{cases} \tag{10}$$

where C_1 is the first encrypted image, and C_2 is the encrypted image after one pixel has been changed in the original image. UACI is calculated as in Eq. (11):

$$\text{UACI} = \frac{1}{nm}\left(\sum_{i,j} \frac{|C_1(i,j) - C_2(i,j)|}{255}\right) \times 100\% \tag{11}$$

where C_1 is the first encrypted image, C_2 is the encrypted image after one pixel in the original file has changed, and n and m are the image's dimensions. The NPCR and UACI values of some test images are shown in Table 3. Given that a successful encryption scheme requires an NPCR value of more than 99% and a UACI value of roughly 33%, it indicates that these values are generally good for our encryption system.

Table 3 NPCR and UACI Values of Encrypted Medical Images

Image	Size	NPCR (%)	UACI (%)
Chest	256×256	99.597215	33.499561
Foot	256×256	99.639773	33.452925
Hand	256×256	99.594175	33.434233
Joint	256×256	99.582016	33.428475

Robustness analysis

Images that are encrypted may suffer harm during network transmission. Even when some data has been lost, a strong encryption scheme should be able to restore the original image. The degree of similarity between the original and decrypted images is measured by the Peak Signal-to-Noise Ratio (PSNR). This value is infinite for the same images. Two images are said to be very similar if the PSNR value converges to infinity; if not, the similarity is low. The PSNR value is determined using Eq. (12) as follows:

$$\text{PSNR} = 10 \times \log_{10}\left(\frac{(255 \times 255)}{\text{MSE}}\right) \quad \text{(dB)} \tag{12}$$

where MSE is the Mean Square Error value between two images, m is the width of the image and n is the height of the image. It is calculated as follows in Eq. (13):

$$\text{MSE} = \frac{1}{mn}\sum_{i=1}^{m}\sum_{j=1}^{n} \|I_1(i,j) - I_2(i,j)\|^2 \tag{13}$$

Cropping attack

A cropping attack substitutes all white or all black values for a portion of the encrypted image. The cropped image is then decrypted, and it is anticipated that the original image will be recovered. The missing data is then evenly spread throughout the entire image. We decrypted the cropped images after applying crop operation at four distinct ratios: 6.25%, 25%, 50%, and 75% of the full image. Despite losing 75% of the original image, our plan was able to restore the original image despite the data loss. Figure 7 lists the results of the cropping assault test, and Table 4 lists the PSNR values. These findings demonstrate how resilient our system is to cropping and data loss attack.

Table 4 PSNR Results Under Cropping Attack

Cropping Ratio	Size	PSNR (dB)
6.25%	256×256	39.876748
25%	256×256	33.914343
50%	256×256	30.909268
75%	256×256	29.150291

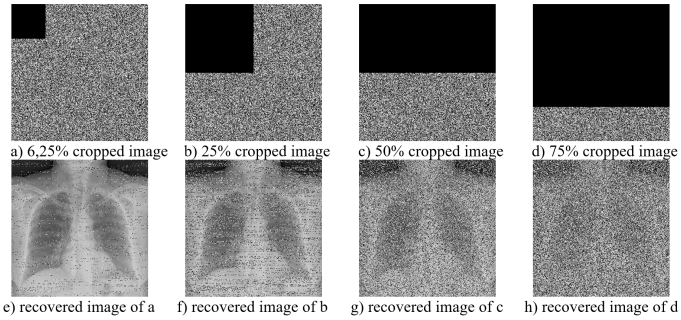

Figure 7 : Cropping attack results.

Noise attack

Some pixels of the encrypted image are randomly altered by noise attacks. Later, the encrypted image with the noise added is decoded. Despite the loss of some data, it is anticipated that the original image will be recovered. For four distinct test images, we injected noise at random in the [1000–1100] pixel range. Figure 8 displays the outcomes of the tests. We show that our approach is quite robust against noise attacks.

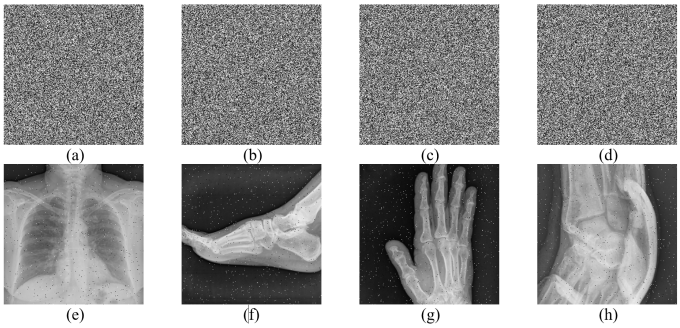

Figure 8 :Noise attack results. a) noise added encrypted image of Chest, b) noise added encrypted image of Foot, c) noise added encrypted image of Hand, d) noise added encrypted image of Joint, e) decrypted image of a, f) decrypted image of b, g) decrypted image of c, h) decrypted image of d.

THE COMPARISON OF SECURITY AND PERFORMANCE ANALYSIS

In this part, we compared our test findings with the study suggested at (Çavuşoğlu *et al.* 2017) using a 256x256 grayscale "crowd" image. They had previously compared the test results of their suggested method with those of other encryption systems using a "crowd" image; we added our test result to the study's table by using the same image. Our test results are added to Table 5 to display the result. In terms of information entropy, NPCR and UACI, our approach outperforms all others.

Table 5 Security and Performance Comparison of Encryption Algorithms

Metric	Chaos (Çavuşoğlu *et al.* 2017)	AES (Çavuşoğlu *et al.* 2017)	Ref. (Çavuşoğlu *et al.* 2017)	Ours
NPCR	99.6067	99.6325	99.6299	99.7021
UACI	31.2477	31.8724	31.8346	33.4502
Entropy	7.9545	7.9591	7.9567	7.9971

In terms of correlation coefficients, information entropy, NPCR, and UACI values, we also compared our approach with those of other studies. To ensure a fair comparison, we used a 512x512 grayscale "Barbara" image, consistent with the other algorithm tests. Table 6 summarizes all the test results. Our scheme outperforms the average of other methods in correlation coefficient values, ranks third in information entropy, holds the second-best NPCR value, and exceeds the average UACI value of the compared algorithms.

Table 6 Performance Comparison Between Our Algorithm and Other Algorithms

Scheme	Corr. H	Corr. D	Corr. V	Entropy	NPCR	UACI
Ref. Wang *et al.* (2019)	-0.0075	-0.0050	0.0040	-	-	-
Ref. Zhou *et al.* (2022)	0.0006	-0.0049	0.0005	7.9977	0.9961	0.3356
Ref. Zhang *et al.* (2019)	-0.0035	0.0025	0.0050	7.9976	0.9962	0.3337
Ref. Machkour *et al.* (2015)	0.0017	0.0023	0.0008	7.9992	0.9981	0.3332
Ref. Wang *et al.* (2016)	-0.0044	-0.0168	0.0198	-	-	-
Ref. Liu and Liu (2020)	-0.0247	-0.0031	-0.0129	7.9942	0.9950	0.3332
Ref. Bakhshandeh and Eslami (2013)	-	-	-	7.9717	0.9956	0.3357
Ref. Zhou (2021)	0.0078	-0.0164	0.0058	7.9974	0.9963	0.3353
Ref. Zhang and Tang (2017)	0.0121	0.0457	0.0389	7.9971	0.9960	0.3343
Ours	0.0045	0.0039	-0.0093	7.9976	0.9966	0.3339

CONCLUSION

This study introduces a chaos-based image encryption algorithm for medical X-ray images. We employed a double Lorenz map: one that is initialized by the secret key and used in the confusion phase, and another that is initialized by the plaintext hash value and secret key and used in the diffusion phase. Row-based and column-based shift operations were used in the confusion phase, while the XOR operation was used in the diffusion phase. To ensure our scheme was stable, resilient, and effective, we thoroughly tested and analyzed it. We evaluated our scheme against similar schemes from previous years and obtained above-average values in terms of NPCR, UACI, information entropy, and correlation coefficient. Our approach outperforms most similar schemes with an average information entropy value of 7.9976, NPCR value of 99.66%, and approximately 33.39% UACI value. All test results demonstrate that our scheme is a very strong security alternative for medical X-ray images.

Ethical standard

The authors have no relevant financial or non-financial interests to disclose.

Availability of data and material

The data that support the findings of this study are available from the corresponding author upon reasonable request.

Conflicts of interest

The authors declare that there is no conflict of interest regarding the publication of this paper.

LITERATURE CITED

Abdelli, A., W. E. h. Youssef, F. Kharroubi, L. Khriji, and M. Machhout, 2024 A novel enhanced chaos based present lightweight cipher scheme. Physica Scripta **99**: 016004.

Alibrahim, H. and S. A. Ludwig, 2021 Image encryption algorithm based on particle swarm optimization and chaos logistic map. In *2021 IEEE Symposium Series on Computational Intelligence (SSCI)*.
Bakhshandeh, A. and Z. Eslami, 2013 An authenticated image encryption scheme based on chaotic maps and memory cellular automata. Optics and Lasers in Engineering **51**: 665–673.
Chai, X., Y. Chen, and L. Broyde, 2017 A novel chaos-based image encryption algorithm using dna sequence operations. Optics and Lasers in Engineering **88**: 197–213.
Chai, X., X. Fu, Z. Gan, Y. Lu, and Y. Chen, 2019 A color image cryptosystem based on dynamic dna encryption and chaos. Signal Processing **155**: 44–62.
Clemente-Lopez, D., J. d. Rangel-Magdaleno, and J. M. Muñoz-Pacheco, 2024 A lightweight chaos-based encryption scheme for iot healthcare systems. Internet of Things **25**: 101032.
Demirkol, A. S., M. E. Sahin, B. Karakaya, H. Ulutas, A. Ascoli, *et al.*, 2024 Real time hybrid medical image encryption algorithm combining memristor-based chaos with dna coding. Chaos, Solitons & Fractals **183**: 114923.
Dua, M. and R. Bhogal, 2024 Medical image encryption using novel sine-tangent chaotic map. e-Prime - Advances in Electrical Engineering, Electronics and Energy **9**: 100642.
Fang, P., H. Liu, C. Wu, and M. Liu, 2021 A secure chaotic block image encryption algorithm using generative adversarial networks and dna sequence coding. Mathematical Problems in Engineering **2021**: 1–26.
Farah, M. B., R. Guesmi, A. Kachouri, and M. Samet, 2020 A novel chaos based optical image encryption using fractional fourier transform and dna sequence operation. Optics & Laser Technology **121**: 105777.
Ismail, S. M., L. A. Said, A. G. Radwan, A. H. Madian, and M. F. Abu-Elyazeed, 2018 Generalized double-humped logistic map-based medical image encryption. Journal of Advanced Research **10**: 85–98.
John, S. and S. Kumar, 2023 2d lorentz chaotic model coupled with logistic chaotic model for medical image encryption: Towards ensuring security for teleradiology. Procedia Computer Science **218**: 918–926.
Kanwal, S., S. Inam, Z. Nawaz, F. Hajjej, H. Alfraihi, *et al.*, 2024 Securing blockchain-enabled smart health care image encryption framework using tinkerbell map. Alexandria Engineering Journal **107**: 711–729.
Kaya, Y., Z. Gurkas-Aydin, and A. Akgul, 2025 A chaos-based lightweight encryption scheme using hash-code and cyclic rotation. Physica Scripta **100**: 045203.
Liu, Q. and L. Liu, 2020 Color image encryption algorithm based on dna coding and double chaos system. IEEE Access **8**: 83596–83610.
Machkour, M., A. Saaidi, and M. L. Benmaati, 2015 A novel image encryption algorithm based on the two-dimensional logistic map and the latin square image cipher. 3D Research **6**.
Malik, M. G., Z. Bashir, N. Iqbal, and M. A. Imtiaz, 2020 Color image encryption algorithm based on hyper-chaos and dna computing. IEEE Access **8**: 88093–88107.
Masood, F., M. Driss, W. Boulila, J. Ahmad, S. u. Rehman, *et al.*, 2021 A lightweight chaos-based medical image encryption scheme using random shuffling and xor operations. Wireless Personal Communications **127**: 1405–1432.
Mohammed, R. A., M. A. A. Khodher, and A. Alabaichi, 2023 A novel lightweight image encryption scheme. Computers, Materials and Continua **75**: 2137–2153.
Oteko Tresor, L. and M. Sumbwanyambe, 2019 A selective image encryption scheme based on 2d dwt, henon map and 4d qi hyper-chaos. IEEE Access **7**: 103463–103472.
Qobbi, Y., A. Abid, M. Jarjar, S. E. Kaddouhi, A. Jarjar, *et al.*, 2023 Adaptation of a genetic operator and a dynamic s-box for chaotic encryption of medical and color images. Scientific African **19**.
Rehman, A. U., A. Firdous, S. Iqbal, A. Zahid, M. M. Shahid, *et al.*, 2020 A color image encryption algorithm based on one time key, chaos theory, and concept of rotor machine. IEEE Access **8**: 172275–172295.
Rehman, M. U., A. Shafique, and A. B. Usman, 2023 Securing medical information transmission between iot devices: An innovative hybrid encryption scheme based on quantum walk, dna encoding, and chaos. Internet of Things **24**: 100891.
Roy, A., D. R. Mahanta, and L. B. Mahanta, 2025 A semi-synchronous federated learning framework with chaos-based encryption for enhanced security in medical image sharing. Results in Engineering **25**: 103886.
Silva Garcia, V. M., M. D. Gonzalez Ramirez, R. F. Carapia, E. Vega-Alvarado, and E. Rodriguez Escobar, 2019 A novel method for image encryption based on chaos and transcendental numbers. IEEE Access **7**: 163729–163739.
Vijayakumar, M. and A. Ahilan, 2024 An optimized chaotic s-box for real-time image encryption scheme based on 4-dimensional memristive hyperchaotic map. Ain Shams Engineering Journal **15**: 102620.
Wang, S., C. Wang, and C. Xu, 2020 An image encryption algorithm based on a hidden attractor chaos system and the knuth–durstenfeld algorithm. Optics and Lasers in Engineering **128**: 105995.
Wang, X., C. Liu, and H. Zhang, 2016 An effective and fast image encryption algorithm based on chaos and interweaving of ranks. Nonlinear Dynamics **84**: 1595–1607.
Wang, X., Y. Wang, X. Zhu, and S. Unar, 2019 Image encryption scheme based on chaos and dna plane operations. Multimedia Tools and Applications **78**: 26111–26128.
Zhang, X., L. Wang, Z. Zhou, and Y. Niu, 2019 A chaos-based image encryption technique utilizing hilbert curves and h-fractals. IEEE Access **7**: 74734–74746.
Zhang, Y. and Y. Tang, 2017 A plaintext-related image encryption algorithm based on chaos. Multimedia Tools and Applications **77**: 6647–6669.
Zhou, S., 2021 A real-time one-time pad dna-chaos image encryption algorithm based on multiple keys. Optics & Laser Technology **143**: 107359.
Zhou, S., Y. Wei, Y. Zhang, and L. Teng, 2022 Novel chaotic image cryptosystem using dynamic dna coding. Research Square Platform LLC .
Çavuşoğlu, , S. Kaçar, I. Pehlivan, and A. Zengin, 2017 Secure image encryption algorithm design using a novel chaos based s-box. Chaos, Solitons & Fractals **95**: 92–101.

How to cite this article: Kaya, Y., and Aydin, Z. G Chaos-Based Encryption Scheme for Secure Medical X-ray Images. *Computers and Electronics in Medicine*, 2(2), 53-59, 2025.